A semi-implicit finite element method for viscous lipidic membranes

Diego S. Rodrigues[a], Roberto F. Ausas[a,b], Fernando Mut[a,*], Gustavo C. Buscaglia[a]

[a]*Instituto de Ciências Matemáticas e de Computação, Universidade de São Paulo, Av. do Trabalhador são-carlense, 400, 13560-970 São Carlos, SP, Brazil*
[b]*IBM Research, Brazil.*

Abstract

A finite element formulation to approximate the behavior of lipidic membranes is proposed. The mathematical model incorporates tangential viscous stresses and bending elastic forces, together with the inextensibility constraint and the enclosed volume constraint. The membrane is discretized by a surface mesh made up of planar triangles, over which a mixed formulation (velocity-curvature) is built based on the viscous bilinear form (Boussinesq-Scriven operator) and the Laplace-Beltrami identity relating position and curvature. A semi-implicit approach is then used to discretize in time, with piecewise linear interpolants for all variables. Two stabilization terms are needed: The first one stabilizes the inextensibility constraint by a pressure-gradient-projection scheme (R. Codina and J. Blasco, Computer Methods in Applied Mechanics and Engineering 143:373-391, 1997), the second couples curvature and velocity to improve temporal stability, as proposed by Bänsch (Numerische Mathematik 88:203-235, 2001). The volume constraint is handled by a Lagrange multiplier (which turns out to be the internal pressure), and an analogous strategy is used to filter out rigid-body motions. The nodal positions are updated in a Lagrangian manner according to the velocity solution at each time step. An automatic remeshing strategy maintains suitable refinement and mesh quality throughout the simulation.

Numerical experiments show the convergent and robust behavior of the proposed method. Stability limits are obtained from numerous relaxation tests, and convergence with mesh refinement is confirmed both in the relaxation transient and in the final equilibrium shape. Virtual tweezing experiments are also reported, computing the dependence of the deformed membrane shape with the tweezing velocity (a purely dynamical effect). For sufficiently

high velocities, a tether develops which shows good agreement, both in its final radius and in its transient behavior, with available analytical solutions. Finally, simulation results of a membrane subject to the simultaneous action of six tweezers illustrate the robustness of the method.
Keywords: Biological Membranes, Lipid Bilayer, Canham-Helfrich Energy, Boussinesq-Scriven Operator, Tangential Calculus, Finite Element.

---

*Corresponding author

Email addresses: diegosarodrigues@gmail.com (Diego S. Rodrigues), rfausas@gmail.com (Roberto F. Ausas), fermut@gmail.com (Fernando Mut), gustavo.buscaglia@icmc.usp.br (Gustavo C. Buscaglia)

1. INTRODUCTION

Phospholipidic membranes are two-molecule-thick curved surface arrays of phospholipids [1] that constitute the fundamental building material of the Living Cell membrane, of many intra-cellular units, and of synthetic vesicles such as liposomes. The static properties of this two-dimensional material are governed by geometry. In fact remarkable agreement with biophysical observations has been obtained with models in which the energy density (per unit area) is a function of the local curvature alone[2, 3]. Such an energy density is typical of *elastic solids* in bending.

Numerical methods for computing equilibrium shapes of these membranes by gradient flow (which in this context is called *Willmore flow*) first appeared about ten years ago, with the works of Dziuk [4], Rusu [5], Feng & Klug [6] and Barret *et al* [7], among others. These methods evolve the geometry by gradient descent towards an equilibrium of the applied forces (if any) with the elastic forces. Bonito *et al* [8, 9] considered the effect of the bulk fluid, while Elliot & Stinner modeled two-phase effects [10], always in gradient flow.

The actual dynamics of phospholipidic membranes does not however obey gradient flow. Their evolution results from the interplay between the applied forces, the hydrodynamic forces coming from the adjacent inner and outer liquids, and the forces that develop on the membrane itself, which include an elastic contribution (as in gradient flow) and also a surface viscous contribution arising from the lipid-to-lipid sliding. In this article we focus just on the membrane forces, restricting the effect of the adjacent liquids to just a volume constraint. The combination of the methods proposed below with more realistic treatments of the inner and outer liquids is straightforward (though the added computational cost is obviously significant).

We assume that the surface viscous forces that develop on the membrane and determine its dynamics correspond to an area-preserving *Newtonian surface fluid* [11, 12, 13]. Our goal is thus to present a finite element method for the *viscous flow* of phospholipidic bilayers; i.e., for the dynamical simulation of phospholipidic bilayers, considering an elastic model for bending deformations and a (viscous) Newtonian area-preserving fluid model for the

dissipative tangential motions.

For this purpose, we adopt the same treatment of elastic forces used for gradient flows[4, 8], combined with a novel treatment of surface viscous forces. The mathematical formulation of surface viscous behavior was first derived by Scriven [14]. Schemes for its numerical approximation have been proposed by Arroyo and coworkers [13, 15, 16] in the axisymmetric case, and by Tasso & Buscaglia [17] in the general 3D case. The formulation of this latter article relies heavily on the numerical differentiation of the energy of the membrane (including an "evanescent elasticity" term which accounts for tangential viscosity) to compute forces and stresses, and on yet another numerical differentiation to compute the approximate tangent matrix. In this work another approach is followed, developing a semi-implicit scheme issued in a classical way from the continuous variational formulation, without adjustable numerical differentiation parameters and involving the solution of just one linear system per time step.

After introducing the mathematical formulation in Section 2 and the proposed discretization scheme in Section 3, we assess the proposed method through numerical examples in Section 4. Special attention is given to experiments that involve membrane tweezing and tether formation. The latter is a salient phenomenon that takes place in phospholipidic bilayers, by which if a small part of a vesicle is pulled away by some localized force (using an optical trap, for example [18]) it carries with it a narrow bilayer tube (tether) that can be much longer that the vesicle itself and nanometric in diameter [19]. The proposed method is shown to be sufficiently robust to allow for accurate simulations of tether formation and extension, which are important to shed light on fundamental mechanisms of cell mechanics [20, 21, 22]. Section 5 is then devoted to summarize the conclusions of the study.

2. MATHEMATICAL FORMULATION

2.1. Virtual power at the interface

We consider the motion of a closed surface $\Gamma \subset \mathbb{R}^3$ under the action of surface elastic forces and external forces coming from the adjacent liquid. The virtual work principle for

such a system reads

$$\int_\Gamma \boldsymbol{\sigma} : D_\Gamma \mathbf{v} = -d\mathcal{E}(\Gamma, \mathbf{v}) + \int_\Gamma \mathbf{f} \cdot \mathbf{v} \qquad \forall\, \mathbf{v} \in V(\Gamma) \tag{1}$$

where $\boldsymbol{\sigma}$ is the tensor of tangential stresses, $\mathcal{E}(\Gamma)$ is the elastic energy from which elastic forces are derived, $\mathbf{f}$ is the net interaction force with the surroundings, $V(\Gamma)$ the space of admissible virtual velocities and $D_\Gamma \mathbf{v}$ the surface virtual strain rate.

In (1), by $d\mathcal{E}(\Gamma, \mathbf{v})$ we denote the derivative (or first variation) of $\mathcal{E}(\Gamma)$ along the virtual velocity field $\mathbf{v}$. In turn, $D_\Gamma \mathbf{v}$ represents the surface differential operator

$$D_\Gamma \mathbf{v} = \frac{1}{2}\, \mathbb{P}\, (\nabla_\Gamma \mathbf{v} + \nabla_\Gamma \mathbf{v}^T)\, \mathbb{P}. \tag{2}$$

which is the surface analog of the usual three-dimensional symmetric gradient $D\mathbf{v} = (\nabla \mathbf{v} + \nabla \mathbf{v}^T)/2$.

Some elements of differential geometry are needed at this point. We follow the presentation of Buscaglia & Ausas [23], the reader is also referred to Biria *et al* [24] for a more comprehensive review.

The tensor $\mathbb{P}$ above is the tangent projector onto Γ given by

$$\mathbb{P} = \mathbb{I} - \breve{\mathbf{n}} \otimes \breve{\mathbf{n}}, \tag{3}$$

$\breve{\mathbf{n}}$ being the normal to Γ, and the symbol ∇_Γ refers to the surface gradient, given by

$$\nabla_\Gamma f = \mathbb{P}\, \nabla \widehat{f} \tag{4}$$

where $\widehat{f}$ is any smooth extension of the function f from its values on Γ to a three-dimensional neighborhood of it. The surface Laplacian $\Delta_\Gamma f$ is defined as $\nabla_\Gamma \cdot (\nabla_\Gamma f)$.

The surface gradient $\nabla_\Gamma \mathbf{w}$ of a vector field $\mathbf{w}$ defined on Γ is defined as the matrix (Cartesian tensor)

$$\{\nabla_\Gamma \mathbf{w}\}_{ij} = \{\nabla_\Gamma w_i\}_j, \tag{5}$$

where w_i is the i-th Cartesian component of $\mathbf{w}$.

2.2. The Boussinesq-Scriven operator

The rheology of a viscous interface Γ is governed by the Boussinesq-Scriven law [14, 25], which is the tangential analog to the Newtonian constitutive law, i.e.,

$$\boldsymbol{\sigma} = (-p_{\mathrm{s}} + \lambda\, \nabla_\Gamma \cdot \mathbf{u})\, \mathbb{P} + 2\,\mu\, D_\Gamma \mathbf{u}, \tag{6}$$

where λ and μ are surface viscosity coefficients, $\mathbf{u}$ is the material velocity of the membrane particles, and p_{s} is a *surface thermodynamic pressure*, which requires a closure law.

An area-preserving membrane (frequently called *inextensible* membrane) is defined by the constraint

$$\nabla_\Gamma \cdot \mathbf{u} = 0 \tag{7}$$

The inextensible limit is obtained making λ tend to infinity. It is a classical result that there exists a *surface pressure* π_{s}, the Lagrange multiplier associated to the constraint (7), such that, irrespective of the closure law for p_{s},

$$\lim_{\lambda \to +\infty} (-p_{\mathrm{s}} + \lambda \nabla_\Gamma \cdot \mathbf{u}) \;\; = \;\; -\pi_{\mathrm{s}}, \tag{8}$$

As a consequence, the tangential stresses from (6) read, for inextensible membranes,

$$\boldsymbol{\sigma} = -\pi_{\mathrm{s}}\, \mathbb{P} + 2\,\mu\, D_\Gamma \mathbf{u}$$

The bilinear form that expresses the virtual power along a virtual velocity field $\mathbf{v}$ performed by the stresses $\boldsymbol{\sigma}$ corresponding to an actual velocity field $\mathbf{u}$ and surface pressure π_{s} is given by

$$\begin{aligned} \mathcal{W}\left((\mathbf{u}, \pi_{\mathrm{s}}), \mathbf{v}\right) &= \int_\Gamma \boldsymbol{\sigma} : D_\Gamma \mathbf{v} \;\; = \\ &= \int_\Gamma 2\,\mu\, D_\Gamma \mathbf{u} : D_\Gamma \mathbf{v} \;\; - \;\; \int_\Gamma \pi_{\mathrm{s}}\, \nabla_\Gamma \cdot \mathbf{v} \end{aligned} \tag{9}$$

Remark: *The bilinear form $\mathcal{W}$ is the surface analog of the Stokes form for bulk fluids, namely*

$$\mathcal{W}^{bulk}\left((\mathbf{u}, p), \mathbf{v}\right) = \int 2\,\mu\, D\mathbf{u} : D\mathbf{v} - \int p\, \nabla \cdot \mathbf{v}$$

with the integrals performed this time over the volume *occupied by the bulk fluid. As it is well known, there is a differential operator that corresponds to* $\mathcal{W}^{bulk}$*, which reads*

$$-\mu\,\nabla^2\mathbf{u} + \nabla p.$$

Similarly, there exists a surface differential operator associated to $\mathcal{W}$*, which can be denoted by*

$$-\mathcal{S}_\Gamma\,\mathbf{u} + \nabla_\Gamma \pi_s,$$

but the actual expression of $\mathcal{S}_\Gamma$ *is quite involved. It can be found in the pioneering work of Scriven [14], which is why* $\mathcal{S}_\Gamma$ *is sometimes referred to as* Boussinesq-Scriven operator*. It can also be found, written in the language of differential forms, in the interesting article by Arroyo & DeSimone [13] (see also [26]).*

2.3. The Canham-Helfrich energy

The elastic bending energy considered here is the simplest version of the model proposed by Canham and Helfrich [2, 27],

$$\mathcal{E}(\Gamma) = \frac{c_{\rm CH}}{2}\int_\Gamma \kappa^2, \tag{10}$$

where $\kappa = \kappa_1 + \kappa_2$ stands for the mean scalar curvature of Γ (κ_1 and κ_2 are the principal curvatures) and $c_{\rm CH}$ is a material dependent parameter. In differential geometry, equation (10) is known as Willmore energy [28].

The Canham-Helfrich energy (10) depends on the shape of Γ and is thus affected by motions along a virtual velocity field $\mathbf{v}$. The derivative of $\mathcal{E}$ along $\mathbf{v}$ was computed by Rusu [5] as

$$d\mathcal{E}(\mathbf{v}) \;=\; c_{\rm CH}\int_\Gamma \left[\frac{|\Delta_\Gamma\boldsymbol{\chi}|^2}{2}\nabla_\Gamma\boldsymbol{\chi} : \nabla_\Gamma\mathbf{v} + \nabla_\Gamma(\Delta_\Gamma\boldsymbol{\chi}) : \nabla_\Gamma\mathbf{v} - 2\,(\nabla_\Gamma(\Delta_\Gamma\boldsymbol{\chi})^T\breve{\mathbf{n}})\cdot(\nabla_\Gamma\mathbf{v}^T\breve{\mathbf{n}})\right] \tag{11}$$

where $\boldsymbol{\chi}$ stands for the identity mapping on Γ (i.e., $\boldsymbol{\chi}(\mathbf{x}) = \mathbf{x},\ \forall\,\mathbf{x}\in\Gamma$), which obeys

$$\mathbb{P} = \nabla_\Gamma\boldsymbol{\chi}, \qquad \text{and} \qquad \boldsymbol{\kappa} \stackrel{\rm def}{=} \kappa\,\breve{\mathbf{n}} = -\Delta_\Gamma\boldsymbol{\chi} \tag{12}$$

89 In terms of the vector curvature $\boldsymbol{\kappa}$, the first variation $d\mathcal{E}(\mathbf{v})$ can be rewritten as

$$d\mathcal{E}(\mathbf{v}) \;=\; c_{\text{CH}} \int_\Gamma \left[\frac{|\boldsymbol{\kappa}|^2}{2} \mathbb{P} : \nabla_\Gamma \mathbf{v} + (\mathbb{I} - 2\,\mathbb{P}) \nabla_\Gamma \mathbf{v} : \nabla_\Gamma \boldsymbol{\kappa} \right] \tag{13}$$

Equivalent formulas were produced by Dziuk [4] and Bonito *et al* [8]. The latter was adopted in our implementation, which reads

$$d\mathcal{E}(\mathbf{v}) \;=\; c_{\text{CH}} \int_\Gamma \left[(\mathbb{I} - 2\,\mathbb{P}) \nabla_\Gamma \mathbf{v} : \nabla_\Gamma \boldsymbol{\kappa} + \frac{1}{2} (\nabla_\Gamma \cdot \mathbf{v}) \, (\nabla_\Gamma \cdot \boldsymbol{\kappa}) \right], \tag{14}$$

which holds if $\boldsymbol{\kappa}$ obeys the weak version of $-\Delta_\Gamma \boldsymbol{\chi} = \boldsymbol{\kappa}$, namely

$$\int_\Gamma \boldsymbol{\kappa} \cdot \boldsymbol{\zeta} = \int_\Gamma \mathbb{P} : \nabla_\Gamma \boldsymbol{\zeta} \qquad\qquad \forall\, \boldsymbol{\zeta} \;\in\; H^1(\Gamma)^3 \tag{15}$$

90 *2.4. Volume and area constraints*

Let $\mathcal{V}$ be the volume enclosed by the lipidic membrane Γ. It satisfies

$$\mathcal{V} = \frac{1}{3} \int_\Gamma \boldsymbol{\chi} \cdot \breve{\mathbf{n}} \tag{16}$$

and its time derivative, when the membrane velocity is $\mathbf{u}$, given by

$$\frac{d\mathcal{V}}{dt} = \int_\Gamma \mathbf{u} \cdot \breve{\mathbf{n}} \tag{17}$$

In general, osmotic equilibrium determines the (fixed) volume $\mathcal{V}^*$ that the surface Γ must enclose at all times along its evolution, so that the instantaneous constraint reads $\int_\Gamma \mathbf{u} \cdot \breve{\mathbf{n}} = 0$. When the membrane evolution is discretized in time, however, the enclosed volume may drift away from the value $\mathcal{V}^*$. To mitigate this error, we implemented a volume controller as follows

$$\int_\Gamma \mathbf{u} \cdot \breve{\mathbf{n}} \;=\; \frac{\mathcal{V}^* - \mathcal{V}}{\tau_v} \tag{18}$$

91 The controller drives the volume towards the target value $\mathcal{V}^*$ with characteristic time τ_v.

Equation (18) acts as an additional constraint on the membrane's dynamics, which materializes as an *internal pressure* p (uniform) which exerts a surface force

$$\mathbf{f}_p = p\, \breve{\mathbf{n}}$$

on Γ.

The area $\mathcal{A}$ of an inextensible membrane is also constant, this time as a consequence of (7) because

$$\frac{d\mathcal{A}}{dt} = \int_\Gamma \nabla_\Gamma \cdot \mathbf{u} = 0. \tag{19}$$

Upon time discretization, as discussed above for the enclosed volume, the restriction $\frac{d\mathcal{A}}{dt} = 0$ may be inexactly satisfied and thus $\mathcal{A}$ may drift away from its correct value $\mathcal{A}^*$. An area controller is thus implemented as

$$\nabla_\Gamma \cdot \mathbf{u} - \frac{\mathcal{A}^* - \mathcal{A}}{\mathcal{A}\,\tau_a} = 0 \tag{20}$$

so that, integrating over Γ, one retrieves

$$\frac{d\mathcal{A}}{dt} \;=\; \frac{\mathcal{A}^* - \mathcal{A}}{\tau_a}$$

which drives the membrane area towards $\mathcal{A}^*$ with characteristic time τ_a.

Remark: *The modifications introduced by the volume and area controllers have no effect* in the exact problem *if the initial volume equals $\mathcal{V}^*$ and the initial area equals $\mathcal{A}^*$. In fact, if $\mathcal{V}(t=0) = \mathcal{V}^*$ then (18) forces $\mathcal{V}(t)$ to equal $\mathcal{V}^*$ at all times. Similarly, if $\mathcal{A}(t=0) = \mathcal{A}^*$, then (20) implies $\mathcal{A}(t) = \mathcal{A}^*$ for all $t > 0$.*

The Lagrange multiplier associated to the conservation of area is the surface pressure π_s, already discussed, so that the area controller adds nothing to the bilinear form (9).

2.5. Variational formulation

Collecting the ingredients discussed in the previous sections, the variational formulation that determines the velocity of the membrane corresponds to the following *linear* problem:

Problem P: *"Find* $(\mathbf{u}, \pi_s, \boldsymbol{\kappa}, p) \in \mathbf{V} \times Q \times \mathbf{K} \times \mathbb{R}$ *such that*

$$\int_\Gamma 2\,\mu\, D_\Gamma \mathbf{u} : D_\Gamma \mathbf{v} \;-\; \int_\Gamma \pi_s\, \nabla_\Gamma \cdot \mathbf{v} \;+$$

$$+\; c_{CH} \int_\Gamma \left[(\mathbb{I} - 2\,\mathbb{P}) \nabla_\Gamma \boldsymbol{\kappa} : \nabla_\Gamma \mathbf{v} + \frac{1}{2} (\nabla_\Gamma \cdot \boldsymbol{\kappa})\, (\nabla_\Gamma \cdot \mathbf{v}) \right] - p \int_\Gamma \mathbf{v} \cdot \breve{\mathbf{n}} \;=\; \int_\Gamma \mathbf{f} \cdot \mathbf{v} \qquad (21)$$

$$\int_\Gamma \xi\, \nabla_\Gamma \cdot \mathbf{u} \;=\; \frac{\mathcal{A}^* - \mathcal{A}}{\mathcal{A}\,\tau_a} \int_\Gamma \xi \qquad (22)$$

$$\int_\Gamma \boldsymbol{\kappa} \cdot \boldsymbol{\zeta} \;=\; \int_\Gamma \nabla_\Gamma \mathbb{P} : \nabla_\Gamma \boldsymbol{\zeta} \qquad (23)$$

$$\int_\Gamma \mathbf{u} \cdot \breve{\mathbf{n}} \;=\; \frac{\mathcal{V}^* - \mathcal{V}}{\tau_v} \qquad (24)$$

for all $(\mathbf{v}, \xi, \boldsymbol{\zeta}) \in \mathbf{V} \times Q \times \mathbf{K}$*."*

The surface pressure π_s, the vector curvature $\boldsymbol{\kappa}$ and the internal pressure p arise in this formulation as "by-products" of computing $\mathbf{u}$. Notice that the force field $\mathbf{f}$ on the right-hand side of (21) now comprises all interaction forces with the surroundings *other than that coming from the internal pressure*. For problem $\mathbf{P}$ to be well-posed, the spaces $\mathbf{V}$, Q and $\mathbf{K}$ need to be discussed.

Assuming the surface Γ to be smooth, which implies that $\boldsymbol{\chi}$ is smooth, one can integrate by parts the right-hand side of (23) so as to take $\mathbf{K} = L^2(\Gamma)^3$. There is then a unique solution $\boldsymbol{\kappa} \in \mathbf{K}$, which can then be seen to be smooth because of the smoothness of $\boldsymbol{\chi}$.

Let us consider then existence and uniqueness of $\mathbf{u}$. For simplicity, let us set $\pi_s = p = 0$ and leave aside Eqs. (22) and (24), which are constraints handled by Lagrange multipliers. All that remains is to plug $\boldsymbol{\kappa}$ into (21) and solve the Boussinesq-Scriven operator to determine $\mathbf{u}$.

The well-posedness of problem $\mathbf{P}$ thus demands that the bilinear form

$$\mathcal{B}(\mathbf{u}, \mathbf{v}) = \int_\Gamma 2\,\mu\, D_\Gamma \mathbf{u} : D_\Gamma \mathbf{v} \qquad (25)$$

be continuous and (weakly) coercive over the velocity space $\mathbf{V}$. For continuity, $\mathbf{V}$ must be contained in $H^1(\Gamma)^3$. For coercivity, it must be quotiented with the space of (infinitesimal)

rigid movements

$$\mathcal{R} \stackrel{\text{def}}{=} \{\mathbf{w} : \mathbb{R}^3 \to \mathbb{R}^3 \mid \mathbf{w}(\mathbf{x}) = \boldsymbol{\omega} \wedge \mathbf{x} + \boldsymbol{\beta},\, \boldsymbol{\omega}, \boldsymbol{\beta} \in \mathbb{R}^3\} \tag{26}$$

because $D_\Gamma \mathbf{w}(\mathbf{x}) = 0$, for all $\mathbf{x}$, whenever $\mathbf{w} \in \mathcal{R}$.

In this exposition we take $\mathbf{V}$ as *equal* to $H^1(\Gamma)^3/\mathcal{R}$ and reason as if the bilinear form $\mathcal{B}(\bullet, \bullet)$ were coercive in $\mathbf{V}$. This assumption allows us to consider $\mathbf{u}$ as uniquely defined by (21), assuming $\boldsymbol{\kappa}$ already computed (and, as said, ignoring the geometrical constraints). Problem **P** is thus assumed to be well-posed, yielding a unique solution $(\mathbf{u}, \boldsymbol{\kappa}) \in \mathbf{V} \times \mathbf{K}$.

Remark: *For later use, let us recall that the energy dissipation rate of the surface is given by*

$$\mathcal{D} = \int_\Gamma 2\mu \, \|D_\Gamma \mathbf{u}\|^2 = \mathcal{B}(\mathbf{u}, \mathbf{u})$$

If we now consider the inextensibility equation (22), the situation is similar to that of the incompressible Stokes equation in that an inf-sup condition arises, namely,

$$\inf_{0 \neq \xi \in Q} \sup_{0 \neq \mathbf{v} \in \mathbf{V}} \frac{\int_\Gamma \xi \, \nabla_\Gamma \cdot \mathbf{v}}{\|\xi\|_Q \, \|\mathbf{v}\|_\mathbf{V}} \; > \; 0 \tag{27}$$

We assume that this condition is fulfilled when $Q = L^2(\Gamma)$.

The reader should be warned that the viscous model above does not incorporate the layer-to-layer slippage of the two molecular sheets that form the lipid bilayer. This mode of deformation may well be dominant in some situations, as discussed by Evans & Yeung [29] and more recently by Rahimi & Arroyo [16]. In this contribution the focus is in the numerical treatment of the Boussinesq-Scriven operator coupled to the Canham-Helfrich elastic model, so that the incorporation of layer-to-layer slippage models is left for future work.

2.6. The evolutionary problem

Up to now we have considered a single instant of time, at which the membrane configuration is described by a surface Γ. Since an outcome of the instantaneous problem is in

fact the velocity field with which the membrane's particles are moving, one is lead to the following evolutionary problem:

Evolutionary problem EP: *"Given* $\Gamma(0)$*, the initial surface, compute the continuous family of surfaces* $\Gamma(t)$ *that evolves from* $\Gamma(0)$ *as convected by the velocity field* $\mathbf{u}(\mathbf{t}) : \mathbf{\Gamma}(\mathbf{t}) \rightarrow \mathbb{R}^{\mathbf{3}}$ *that solves problem P. In mathematical terms, the family* $\Gamma(t)$ *must satisfy*

$$\forall \mathbf{x} \in \Gamma(t), \;\; dist\,(\mathbf{x} + \mathbf{u}(\mathbf{x}, t)\,\delta\,t, \Gamma(t + \delta t)) \;\; \leqslant C\,\delta t^2 \tag{28}$$

where dist stands for the distance between a point and a surface, for some $C > 0$*.*

Notice that the tangential component of $\mathbf{u}(t)$ is inconsequential in the evolution of $\Gamma(t)$. However, and contrary to what happens in gradient flow, the tangential velocity generated by viscous flow is *not* zero.

3. DISCRETIZATION

We consider triangulation surfaces in 3D space, which for a fixed mesh connectivity are uniquely described by the vector $\underline{\mathbf{X}}$ of vertex positions. Time is discretized so that a sequence of triangulation surfaces Γ^0, Γ^1,...,Γ^n,... are computed, corresponding to vertex positions $\underline{\mathbf{X}}^0$, $\underline{\mathbf{X}}^1$,...,$\underline{\mathbf{X}}^n$,....

On each Γ^n we define the piecewise-affine finite element space

$$\mathbb{P}_1^n = \{f \in \mathcal{C}^0(\Gamma^n) \;:\; f|_K \text{ is affine, } \forall\, K \text{ triangle in } \Gamma^n\} \tag{29}$$

and the approximation spaces for velocity, surface pressure and curvature

$$\mathbf{V}_h^n = (\mathbb{P}_1^n)^3 \,/\, \mathcal{R} \tag{30}$$

$$Q_h^n = \mathbb{P}_1^n \tag{31}$$

$$\mathbf{K}_h^n = (\mathbb{P}_1^n)^3 \tag{32}$$

DISCRETE PROBLEM DP: Defining $\delta t = t_{n+1} - t_n$, the proposed scheme updates the nodal positions in a Lagrangian way, i.e.,

$$\mathbf{X}^{J,n+1} = \mathbf{X}^{J,n} + \delta t\, \mathbf{u}_h^{n+1}(\mathbf{X}^{J,n}) \tag{33}$$

where J is the nodal index, so that (28) is by construction satisfied. Notice that the velocity field $\mathbf{u}_h^{n+1}$ is computed on Γ^n and is thus an element of $\mathbf{V}_h^n$.

The fully discrete linear problem that determines $\mathbf{u}_h^{n+1}$ is the following:

"Find $(\mathbf{u}_h^{n+1}, \pi_h^{n+1}, \boldsymbol{\kappa}_h^{n+1}, p^{n+1}) \in \mathbf{V}_h^n \times Q_h^n \times \mathbf{K}_h^n \times \mathbb{R}$ *such that*

$$\begin{aligned}
\int_{\Gamma^n} 2\,\mu\, D_\Gamma \mathbf{u}_h^{n+1} : D_\Gamma \mathbf{v} \; + \int_{\Gamma^n} \pi_h^{n+1}\, \nabla_\Gamma \cdot \mathbf{v} \;\; - \; p^{n+1} \int_{\Gamma^n} \mathbf{v} \cdot \breve{\mathbf{n}} \, + \\
+ \;\; c_{CH} \int_{\Gamma^n} \left[(\mathbb{I} - 2\,\mathbb{P}) \nabla_\Gamma \mathbf{v} : \nabla_\Gamma \boldsymbol{\kappa}_h^{n+1} + \frac{1}{2} (\nabla_\Gamma \cdot \mathbf{v})\, (\nabla_\Gamma \cdot \boldsymbol{\kappa}_h^{n+1}) \right] &= \int_{\Gamma^n} \mathbf{f}^{n+1} \cdot \mathbf{v} \qquad (34) \\
\int_{\Gamma^n} \xi\, \nabla_\Gamma \cdot \mathbf{u}_h^{n+1} + \int_{\Gamma^n} \gamma_h\, (\nabla_\Gamma \pi_h^{n+1} - \mathbf{g}_h^n) \cdot \nabla_\Gamma \xi &= \frac{\mathcal{A}^* - \mathcal{A}^n}{\mathcal{A}^n\, \tau_a} \int_{\Gamma^n} \xi \qquad (35) \\
- \int_{\Gamma^n} \tau_\kappa \nabla_\Gamma \mathbf{u}_h^{n+1} : \nabla_\Gamma \boldsymbol{\zeta} + \int_{\Gamma^n} \boldsymbol{\kappa}_h^{n+1} \cdot \boldsymbol{\zeta} &= \int_{\Gamma^n} \mathbb{P} : \nabla_\Gamma \boldsymbol{\zeta} \qquad (36) \\
\int_{\Gamma^n} \mathbf{u}_h^{n+1} \cdot \breve{\mathbf{n}} &= \frac{\mathcal{V}^* - \mathcal{V}^n}{\tau_v} \qquad (37)
\end{aligned}$$

hold $\forall \mathbf{v} \in \mathbf{V}_h^n$, $\forall \xi \in Q_h^n$ *and* $\forall \boldsymbol{\zeta} \in \mathbf{K}_h^n$*."* Together with (33), this completely defines the fully discrete formulation. Notice that all integrals are performed over the known discrete surface Γ^n.

Several remarks are in order:

- Algorithms that compute the velocity with frozen vertex positions, as is the case of **DP**, suffer severe stability restrictions on δt. The trend has thus been to "implicitize" as many terms as possible while keeping the problem to be solved at each time step linear, as done by Rusu [5], Dziuk [4] and others.

- A stabilization term
$$\int_{\Gamma^n} \gamma_h\, (\nabla_\Gamma \pi_h^{n+1} - \mathbf{g}_h^n) \cdot \nabla_\Gamma \xi$$
has been added in the inextensibility equation (35). This aims at stabilizing checkerboard modes arising from the equal-order interpolation of $\mathbf{u}_h$ and π_h. The stabilization technique is taken from the "stabilization by pressure gradient projection" method proposed by Codina & Blasco [30, 31, 32]. The vector field $\mathbf{g}^n$ is the $L^2(\Gamma)$-projection of

$\nabla_\Gamma \pi_h^n$ onto $(Q_h^n)^3$, i.e.,

$$\int_{\Gamma^n} \mathbf{g}_h^n \cdot \mathbf{v} = \int_{\Gamma^n} \nabla_\Gamma \pi_h^n \cdot \mathbf{v} \qquad \forall\, \mathbf{v} \in (Q_h^n)^3 \tag{38}$$

The parameter γ_h varies from element to element, according to

$$\gamma_h = \frac{h_K^2}{10\,\mu} \tag{39}$$

where h_K is the diameter of element K. The consistent mass matrix is used in solving (38).

- By comparing (36) to its exact version (23), one notices the addition of the stabilization term due to Bänsch [33]

$$-\int_{\Gamma^n} \tau_\kappa \nabla_\Gamma \mathbf{u}_h^{n+1} : \nabla_\Gamma \boldsymbol{\zeta}_h$$

for which the usual choice is $\tau_\kappa = \delta t$, adopted throughout this article. This term significantly increases the temporal stability. It allows time steps hundreds of times larger than those allowed by the unstabilized algorithm ($\tau_K = 0$).

- The space $\mathbf{V}_h^n$ needs to have its rigid modes filtered out. We accomplish this by a classical Lagrange multiplier technique, which adds 6 equations ($\int_{\Gamma^n} \mathbf{u}_h^{n+1} = \mathbf{0}$ and $\int_{\Gamma^n} \mathbf{x} \wedge \mathbf{u}_h^{n+1} = \mathbf{0}$) and 6 unknowns to the global matrix.

- The characteristic times τ_a and τ_v of the area and volume controllers, respectively, which are non-physical, are taken as

$$\tau_a \;=\; \tau_v \;=\; 10\,\delta t \tag{40}$$

This choice yields the best results in terms of accuracy and stability, as concluded from numerous experiments.

4. REMESHING

The simulation of evolving surfaces that undergo large deformations requires adaptive meshing techniques to mantain good accuracy along the computations. The loss of acuracy

is not only related to the degradation of triangles quality, but also to the changes in time of the local surface curvature. In order to cope with these issues an automatic discrete surface regridding software was employed [34].

The remeshing procedure starts by defining a single discrete patch as the whole support surface whose boundary is the largest edge. Using this edge as the initial front, the discrete patch is triangulated using an advancing front technique. The desired local element size is defined using the curvature information by the rule

$$h^*(\kappa) = \frac{c_h}{\kappa} \qquad ,$$

where c_h is a user-defined parameter, and κ is the scalar curvature provided by the field solver. The specified element size is isotropic since only scalar curvature information is used. The output of this step is a completely new discrete surface. Although the new nodes lie on the original surface, the two surfaces are not coincident. In particular, discrepancies in the curvature introduce discontinuities in the elastic energy after each remeshing. These perturbations are however rapidly dissipated and seem to not have any major impact on the simulation results.

In order to assess the quality of a given surface discretization, two parameters are defined as measures of the shape and size quality of each individual triangle K as follows:

- Element *shape* quality:

$$q_K^{\text{shape}} = (12\sqrt{3})\, A_K / P_K^2,$$

  where A_K and P_K are the triangle's area and perimeter, respectively.

- Element *size* quality:

$$q_K^{\text{size}} = \min\left\{\frac{h^*(\kappa_K)}{h_K}, 1\right\}$$

Global measures of shape and size qualities are then defined as

$$Q_{\text{shape}} = \min_K \{q_K^{\text{shape}}\} \qquad \text{and} \qquad Q_{\text{size}} = \min_K \{q_K^{\text{size}}\}$$

respectively.

The evolving discrete surface is remeshed every time one of the two quality measures drops below given threshold values (Q^*_{shape} and Q^*_{size}). For all the simulations presented in this paper Q^*_{shape} and Q^*_{size} were set to 0.65 and 0.55 respectively.

5. NUMERICAL RESULTS

5.1. Adimensionalization

It is convenient to express the numerical results in non-dimensional form. For this purpose, one defines the basic length scale for an inextensible membrane as

$$R_0 = \sqrt{\frac{\mathcal{A}}{4\,\pi}}$$

so that the non-dimensional area is always $4\,\pi$. This allows for the definition of consistent scales for velocity, surface pressure, surface stress, curvature, internal pressure and other variables as shown in Table 1.

A *relaxation experiment* corresponds to solving problem **P** repeatedly starting from an initial configuration Γ^0 and with no forces other than the internal pressure applied (i.e.; $\mathbf{f} = 0$), so that the membrane evolves towards a nearby equilibrium. In a relaxation experiment all non-dimensional variables depend just on the non-dimensional initial configuration $\widehat{\Gamma}^0$, where $\widehat{\Gamma}^0$ is the scaled version of Γ^0, i.e.;

$$\mathbf{x} \in \Gamma^0 \;\Leftrightarrow\; \widehat{\mathbf{x}} \stackrel{\text{def}}{=} \frac{1}{R_0}\,\mathbf{x} \;\in \widehat{\Gamma}^0 \tag{41}$$

If two relaxation experiments share the same $\widehat{\Gamma}^0$, then the time history (in terms of non-dimensional time) of all (non-dimensional) variables must coincide, irrespective of the actual values of R_0, c_{CH} and μ.

In a *tweezing experiment*, on the other hand, there is a part of the membrane that is pulled away with some imposed velocity V_T or some imposed force F_T. In this case the non-dimensional solutions will depend both on $\widehat{\Gamma}^0$ and on the non-dimensional value of the imposed velocity or force, which acts as an additional non-dimensional parameter.

In what follows, all reported quantities are non-dimensional unless explicitly said otherwise. The sample values tabulated above may help the reader in translating the non-dimensional results into physical quantities.

Quantity	**Symbol**	**Scale**	**Sample value**
Space	$\mathbf{x}$	R_0	10^{-6} m
Time	t	$\frac{\mu R_0^2}{c_{\text{CH}}}$	0.25 s
Velocity	$\mathbf{u}$	$\frac{c_{\text{CH}}}{\mu R_0}$	4×10^{-6} m/s
Area	$\mathcal{A}$	R_0^2	10^{-12} m^2
Energy	$\mathcal{E}$	c_{CH}	4×10^{-20} J
Dissipation	$\mathcal{D}$	$\frac{c_{\text{CH}}^2}{\mu R_0^2}$	1.6×10^{-19} W
Surface pressure	π_s	$\frac{c_{\text{CH}}}{R_0^2}$	4×10^{-8} Pa-m
Surface stress	$\boldsymbol{\sigma}$	$\frac{c_{\text{CH}}}{R_0^2}$	4×10^{-8} Pa-m
Curvature	$\boldsymbol{\kappa}$	$\frac{1}{R_0}$	10^6 m^{-1}
Internal pressure	p	$\frac{c_{\text{CH}}}{R_0^3}$	0.04 Pa
Surface force	$\mathbf{f}$	$\frac{c_{\text{CH}}}{R_0^3}$	0.04 Pa
Force	F	$\frac{c_{\text{CH}}}{R_0}$	4×10^{-14} N

Table 1: Adimensionalization scales for the intervening variables. The sample values correspond to $R_0 = 10^{-6}$ m, $c_{\text{CH}} = 4 \times 10^{-20}$ J and $\mu = 10^{-8}$ Pa-s-m.

5.2. Relaxation experiments: Stability limit, convergence and equilibrium shape

Equilibrium shapes of lipidic membranes, or equivalently stationary points (local minima) of the Canham-Helfrich energy, are configurations Γ^∞ at which the membrane is in static equilibrium (the solution to problem $\mathbf{P}$ is $\mathbf{u}(\mathbf{x}) = 0\,\forall \mathbf{x} \in \Gamma$). Equilibrium shapes have been studied extensively by Seifert and coworkers [3], among others.

The *viscous relaxation* of a membrane corresponds to the evolution, without any external force ($\mathbf{f} \equiv 0$), from an initial shape Γ^0 towards an equilibrium shape Γ^∞, obeying the viscous model described in this article. In what follows we assess the performance of the proposed method (defined by Eqs. (33)-(37)) for relaxation experiments. For this purpose, we first determine the stability limit of the method (maximum δt for stable behavior, as a function of the mesh size), and then conduct numerical relaxations with increasingly refined meshes. There is no analytical solution for the relaxation transient, so that what is being analyzed is the consistency of the results obtained for different meshes. The discrete equilibrium shape, on the other hand, can be compared to quasi-analytical results (analogous to those of Veerapaneni *et al* [35]).

5.2.1. Stability limits

The initial shape can be seen in Figure 1, with a triangulation that corresponds to the finest mesh employed (mesh MR3). The enclosed volume is $\mathcal{V}(t = 0) = 3.1907$, and this same value is taken as $\mathcal{V}^*$. Though this value is non-dimensional, it is customary to express the volume in terms of another non-dimensional quantity, the *reduced volume* [3]

$$v \stackrel{\text{def}}{=} \frac{6\sqrt{\pi}\,\text{Volume}}{\text{Area}^{\frac{3}{2}}} = \frac{3\,\mathcal{V}}{4\,\pi} \tag{42}$$

where "Volume" and "Area" stand for the actual (dimensional) volume enclosed by the membrane and area of the membrane, respectively. The reduced volume enclosed by mesh MR3 is $v(t = 0) = 0.7617$.

All results below and in the next sections are computed with algorithm DP (Equations (33)-(37)), with $\tau_K = \delta t$, $\tau_a = \tau_v = 10\,\delta t$ and γ_h given by (39).

The first experiments aim at determining the maximum time step size δt_{lim} for which the fully-discrete method DP behaves in a stable way. For this purpose, one hundred time

steps are run on each mesh for several choices of δt. Unstable runs are easily recognizable by violent fluctuations of the elastic energy and of the maximum velocity. The limit value δt_{lim} is obtained by dychotomic search with a tolerance $\leqslant 20\%$.

Three increasingly refined triangulations are employed, of which the most refined is the already described mesh MR3. The maximum time steps allowed by the method can be observed in Table 2. They obey the formula

$$\delta t_{\text{lim}} \;\simeq\; 0.42\, h_{\text{min}}^2 \tag{43}$$

almost exactly. Notice that this formula is non-dimensional, expressed dimensionally it reads

$$\delta t_{\text{lim}} \;\simeq\; \frac{0.42\,\mu}{c_{\text{CH}}}\, h_{\text{min}}^2 \qquad \text{(dimensionally)}.$$

The constant 0.42 can of course depend on the shape of the membrane, so that a similar study was performed on several very different shapes and with uniform or adaptively refined triangulations. The δt_{lim} obtained for each initial mesh is plotted as a function of h_{min} in Figure 1.

The best-fit line in magenta corresponds to (43), which as observed from the plot in some cases overestimates δt_{lim}. Further, we have observed quite often that choosing δt very close to the stability limit deteriorates the accuracy of the computations. This could be a consequence of the term $\int_{\Gamma^n} \tau_K \nabla_\Gamma \mathbf{u}_h^{n+1} : \nabla_\Gamma \boldsymbol{\zeta}$ in (36), since we are taking $\tau_K = \delta t$. For these two reasons we adopt as automatic time-step determination formula (*adjusted every single time step*) one fourth of the value given by (43), that is,

$$\delta t \;=\; \delta t^*(h_{\text{min}}) \;\stackrel{\text{def}}{=}\; 0.105\, h_{\text{min}}^2. \tag{44}$$

Unless otherwise stated, all relaxation experiments described below have been conducted with this time-stepping strategy.

5.2.2. Convergence of relaxation dynamics

Let us assess now the convergence of the proposed method. The initial meshes are MR1, MR2 and MR3, and the time step is updated according to (44). The initial values of the

Mesh	# nodes	# elements	$h_{\min}$	$\delta t_{\lim}$
MR1	592	1180	0.041	7.0×10^{-4}
MR2	2177	4350	0.021	1.6×10^{-4}
MR3	8126	16248	0.010	4.2×10^{-5}

Table 2: Maximum time step for stable behavior of the method, as obtained for each of the meshes of the relaxation study.

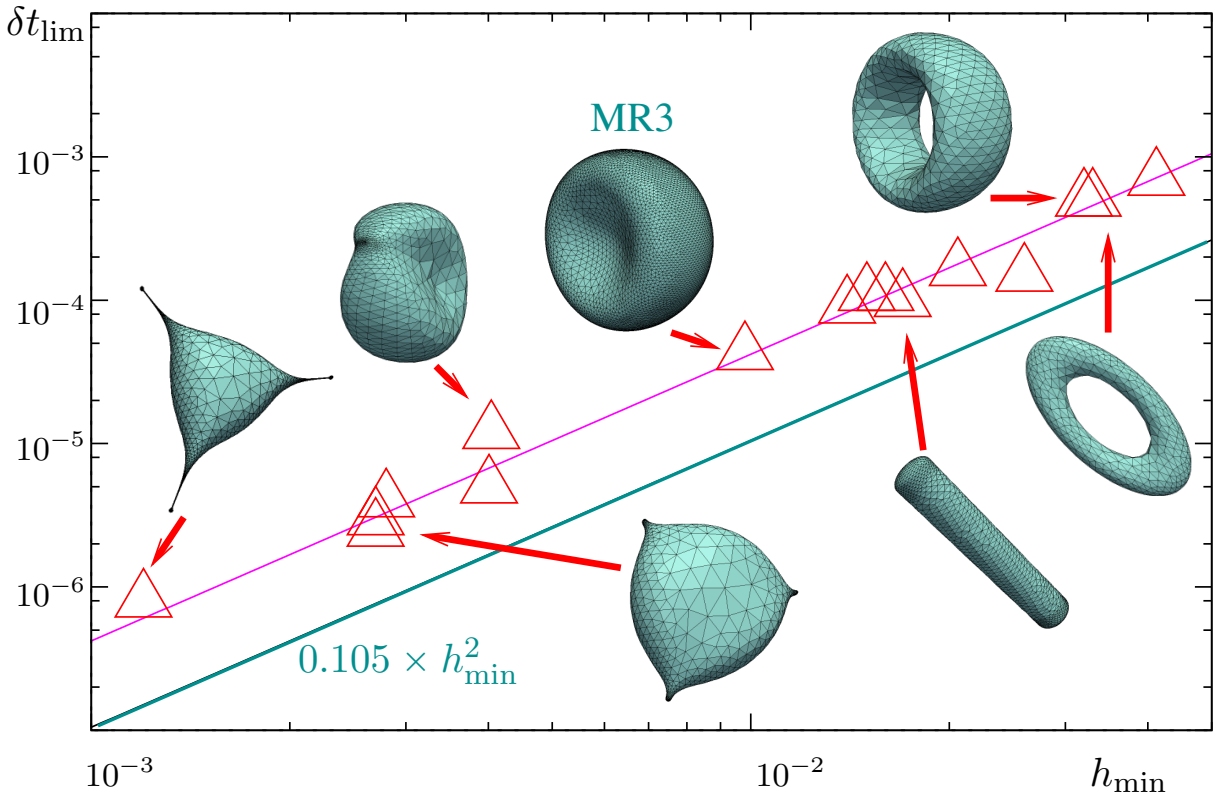

Figure 1: Stability limit δt_{lim} plotted as a function of the minimum edge size h_{min}. The triangles are experimentally obtained values for meshes of different shapes and refinement (some of the shapes are shown and the corresponding data point indicated). In magenta the best-fit line $0.42\, h_{\mathrm{min}}^2$. In cyan the adopted time-stepping strategy, $0.105\, h_{\mathrm{min}}^2$.

time step are, thus, 1.75×10^{-4}, 0.40×10^{-4} and 1.05×10^{-5}. The simulated non-dimensional time is 0.06.

There is no analytical solution for this evolutionary problem, so that the experiments aim at checking the consistency of the results with mesh (and time step) refinement.

In Fig. 2 we plot several integral quantities of the relaxation process, namely the (all non-dimensional) energy $\mathcal{E}$, the internal pressure p, the dissipation rate $\mathcal{D}$, and the $L^2(\Gamma)$ norms of the velocity $\mathbf{u}$ and of the surface pressure π_s, as functions of non-dimensional time t. The shape evolution is shown at the top of the Figure.

The relaxation process is seen to take until about $t = 0.06$, with an energy reduction of about 20% (from ~ 49 to ~ 39). The consistency of the curves corresponding to MR1, MR2 and MR3, and the close agreement between the two finest meshes, provide strong evidence of mesh convergence. Notice how some spurious transient that takes place at $t \simeq 0.03 - 0.04$ for mesh MR1 (especially evident in the plot of $\|\mathbf{u}\|_2$) completely disappears after mesh refinement.

5.2.3. Equilibrium shapes

Discrete equilibrium shapes can be obtained by gradient flow or by viscous flow, once the evolutionary problem reaches its steady state. It is an important consistency check for the proposed method that the discrete equilibrium shapes it provides are indeed approximations of exact equilibrium shapes.

To perform this check, quasi-analytical solutions were computed for axisymmetric shapes by numerically integrating the associated system of ODEs with an extremely fine discretization. In this way, axisymmetrical versions of the quasi-analytical shapes produced by Veerapaneni *et al* [35] were obtained. They can be compared to the numerical shapes at which the algorithm arrives after the relaxation process. We selected for this comparison oblate equilibrium shapes with reduced volumes of $v = 0.61$ and $v = 0.81$. For each reduced volume, three increasingly refined meshes were used, as in the previous section (in fact, essentially the same meshes).

To compare the 3D results with the axisymmetric solution, the symmetry axis of the

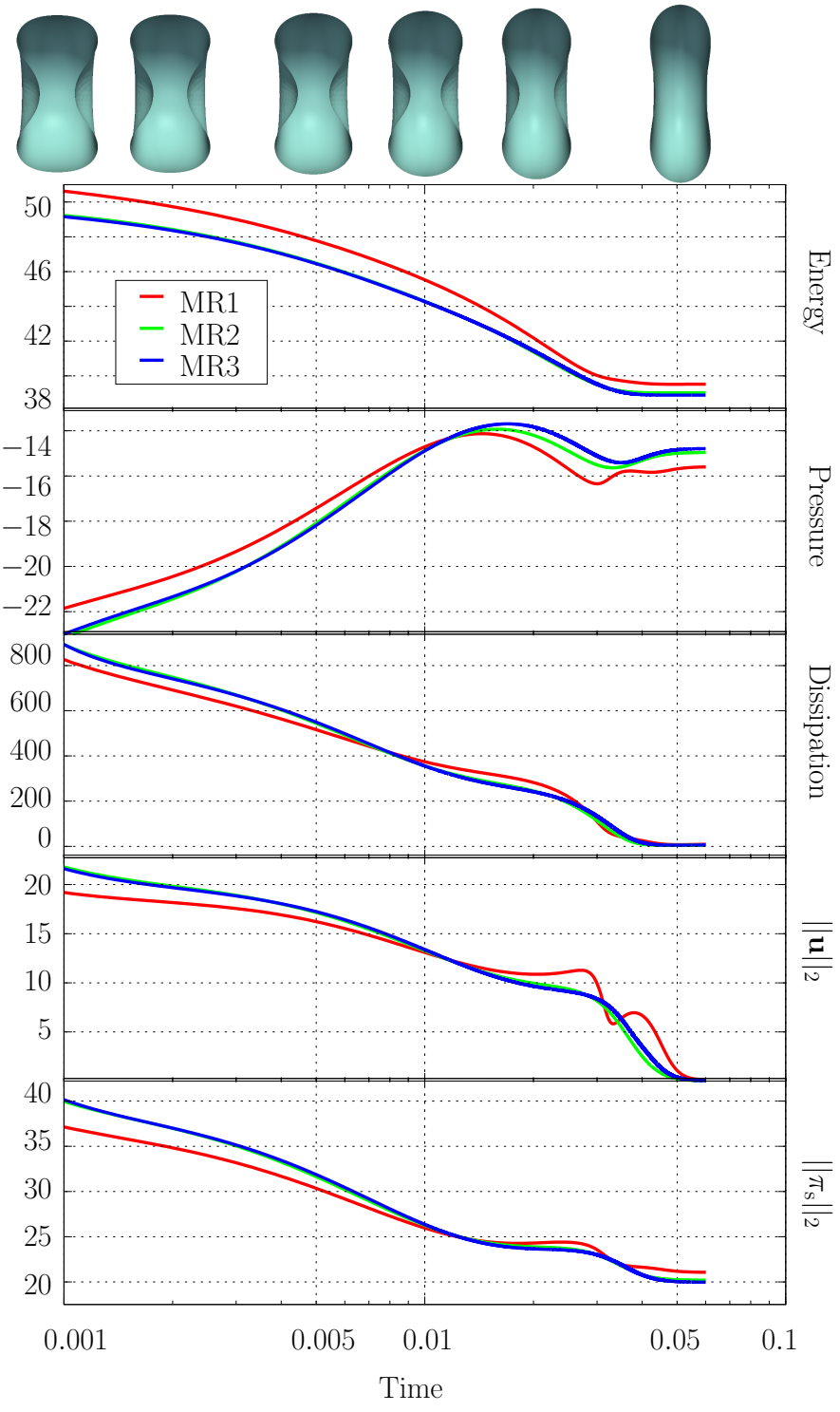

Figure 2: Time evolution of energy, internal pressure, dissipation, velocity norm and surface pressure norm (both in $L^2(\Gamma)$) along the relaxation experiment. The different colors correspond to the increasingly refined meshes MR1, MR2 and MR3. On top, the shape of the membrane at different instants (the horizontal position of each shape approximately corresponds to its time).

3D mesh is identified by diagonalizing the tensor $\int_\Gamma \mathbf{x}\otimes\mathbf{x}$, and so a cylindrical coordinate system $r-z-\phi$ can be assigned to each point in Γ, and also an arc-length coordinate s along the meridians.

In Figure 3(a) the $r-z$ coordinates of the nodes of the *coarsest* relaxed mesh are superposed to the corresponding quasi-analytical curves (just one fifth of the nodes are plotted, to leave the exact curve visible). Just the results of the equilibrium shape corresponding to $v=0.61$ are shown, since those of $v=0.81$ are analogous. The shape is seen to be quite correctly reproduced. To compare the curvature, we plot it as a function of the arc-length coordinate in Figure 3(b). Each data point of these figures involves an error, from which we compute

$$\mathrm{err}(\mathbf{x}) = \left[\frac{1}{\#\text{ nodes}}\sum_{J\,\in\,\text{nodes}} \|\mathbf{X}^J - \mathtt{cp}(\mathbf{X}^J)\|^2\right]^{\frac{1}{2}}$$

where $\mathtt{cp}(\mathbf{x})$ is the closest projection of $\mathbf{x}$ onto the exact equilibrium shape Γ. In the same way, comparing the numerical nodal values of the different quantities to their exact value at the closest point of Γ, we compute discrete estimates of the errors of the different fields, i.e., $\mathrm{err}(\breve{\mathbf{n}})$, $\mathrm{err}(\boldsymbol{\kappa})$, $\mathrm{err}(\kappa)$, $\mathrm{err}(\pi_s)$.

The results are summarized in Table 3 for the two reduced volumes $v=0.61$ and $v=0.81$. One observes convergent behaviors of order $\mathcal{O}(h^{5/3})$ for the position and $\mathcal{O}(h^{3/2})$ for the vector curvature $\boldsymbol{\kappa}$, which are the main unknowns of the problem. The surface pressure π_s seems to converge with first order, while internal pressure p and the elastic energy $\mathcal{E}$ seem to be second order.

It is interesting that the algorithmic normal $\breve{\mathbf{n}}$, numerically computed as $\boldsymbol{\kappa}_h/\kappa_h$, converges with less accuracy than $\boldsymbol{\kappa}$ itself. In Fig. 3(c)-(d) we plot the error distribution of $\boldsymbol{\kappa}$ and of $\breve{\mathbf{n}}$ as a function of the arc-length coordinate. Notice how the error in $\breve{\mathbf{n}}$ concentrates at regions where the mean curvature takes values close to zero.

5.2.4. Mesh distortions near equilibrium

The remeshing process is important in the long term stability of the method. In relaxation simulations, once the shape has minimized its energy there still persists a small

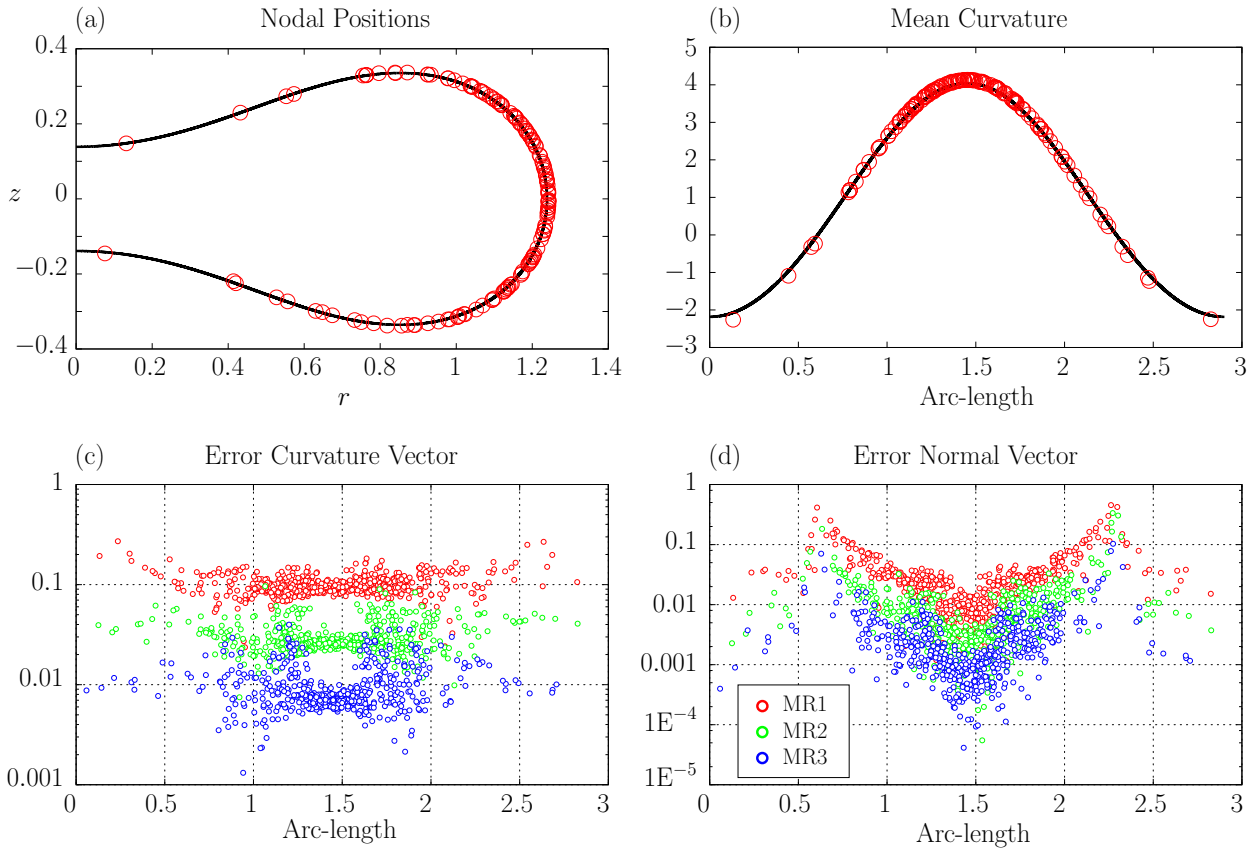

Figure 3: Numerical and quasi-analytical equilibrium shapes for $v = 0.61$. (a) Coordinates $r - z$ of nodal positions (red circles) and exact shape (black line). (b) Mean curvature at the nodes as a function of the meridian-arc length (red circles) and exact mean curvature (black line). (c) Nodal errors of the curvature vector $\boldsymbol{\kappa}_h$ as a function of the meridian-arc length for the three meshes MR1 (red), MR2 (green) and MR3 (blue). (d) Idem as (c) for the normal vector $\breve{\mathbf{n}}_h$.

Case $v = 0.6104$ ($p = -15.61$, $\mathcal{E} = 48.47$)

mesh	$h_{\min}$	err($\mathbf{x}$)	err($\breve{\mathbf{n}}$)	err($\boldsymbol{\kappa}$)	err(κ)	err(π_s)	err(p)	err($\mathcal{E}$)
MR1	0.04	2.91e-03	1.21e-01	1.04e-01	7.34e-02	6.26e-01	5.1581e-01	5.7932e-01
MR2	0.02	8.45e-04	3.43e-02	3.25e-02	1.99e-02	2.34e-01	1.4022e-01	1.5458e-01
MR3	0.01	2.68e-04	2.59e-02	1.23e-02	5.38e-03	1.55e-01	3.7460e-02	3.8833e-02
EOC		1.67	1.08	1.50	1.83	0.98	1.84	1.90

Case $v = 0.8101$ ($p = -14.39$, $\mathcal{E} = 35.89$)

mesh	$h_{\min}$	err($\mathbf{x}$)	err($\breve{\mathbf{n}}$)	err($\boldsymbol{\kappa}$)	err(κ)	err(π_s)	err(p)	err($\mathcal{E}$)
MR1	0.04	2.61e-03	1.48e-01	5.41e-02	3.90e-02	5.74e-01	3.92e-01	1.49e-01
MR2	0.02	7.54e-04	4.43e-02	1.62e-02	1.05e-02	1.74e-01	1.08e-01	3.52e-02
MR3	0.01	2.55e-04	2.52e-02	6.02e-03	2.80e-03	8.12e-02	2.91e-02	5.36e-03
EOC		1.63	1.24	1.54	1.85	1.37	1.83	2.34

Table 3: Experimental convergence analysis of the different variables as compared to those of the exact shapes for $v = 0.61$ and $v = 0.81$. EOC stands for "estimated order of convergence".

velocity field on the membrane. These velocities, arguably similar to the parasitic velocities that appear in capillary flows [36, 37, 38, 39, 40], slowly distort the mesh until some sort of instability is triggered and the simulation diverges.

An attempt to illustrate this phenomenon is made in Figure 4. There the evolution of the energy and of the mesh quality along a relaxation simulation are plotted. The relaxation should end at $t \simeq 0.06$, with the velocity going to zero and the membrane remaining forever after in the equilibrium configuration. One observes, however, that the quality of the mesh deteriorates steadily and the elastic energy begins to grow after $t \simeq 0.07$. This behavior, if allowed to progress, completely pollutes the simulation. The dotted curves after $t = 0.1$ correspond to the evolutions of energy and mesh quality that would be obtained if the remeshing operation automatically activated at $t = 0.1$ were inhibited. The mesh distortions in these instabilities are more pronounced in some localized region. The inserts in Figure 4 show the affected region at the time of remeshing and sometime later, in a non-remeshed simulation.

After remeshing at $t = 0.1$ there is a slight adjustment of the energy due to the change in mesh and then again a state of pseudo-rest develops, in which nothing happens other than a slow distortion of the nodal positions. After time $t \simeq 0.3$ this spurious movement begins to significantly affect mesh quality and the energy begins to grow again. A new instability develops quite similar to the one that activated the first remeshing, leading to a second remeshing at $t \simeq 0.36$. The inserts show the critical regions, exhibiting the unstable distortion pattern.

Remeshing is thus seen to serve not just as a mesh adaptation strategy, but also as a control mechanism for spurious unstable distortions.

5.3. Tethering experiments: Membrane tweezing, dynamical effects

5.3.1. Basic description

A tether develops when a small parcel of the membrane is pulled away. If a force F_T is applied to the parcel, a structure develops composed of a head, a cylindrical tube of length $L(t)$ and radius $R(t)$ and the connection to the membrane body as shown in Figure 5.

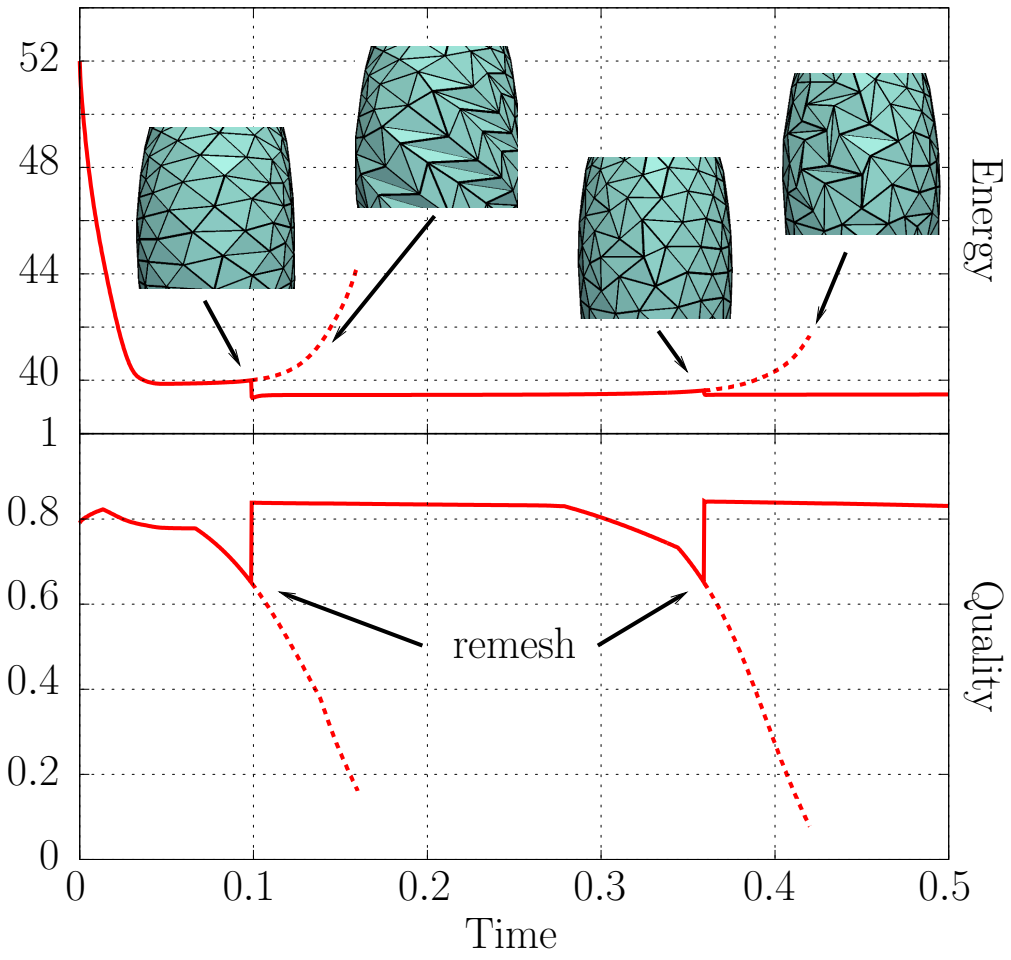

Figure 4: Long-term evolution of a relaxing membrane. Plotted are the elastic energy and mesh quality as functions of time. The state of rest is not completely achieved and small parasitic velocities distort the mesh activating the remeshing process. The dotted lines show the evolution of the variables if remeshing is inhibited, and the inserts show the unstable distortion pattern.

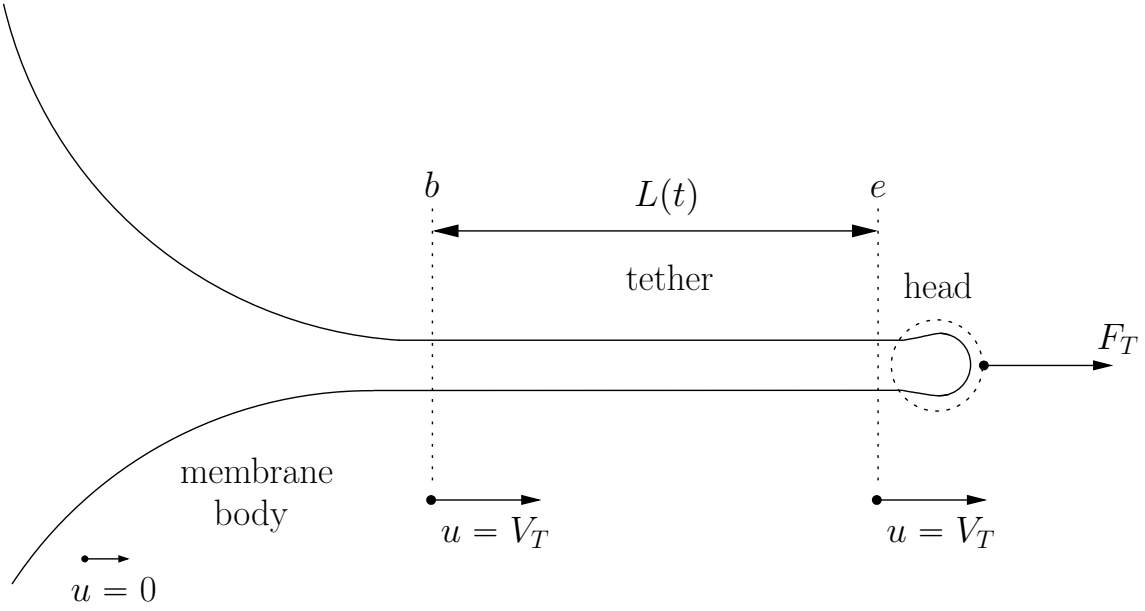

Figure 5: Schematics of membrane tethering.

The dynamics of the tether can be understood with the help of the analytical solution corresponding to a (circular) cylindrical inextensible membrane. We here go back to dimensional quantities and consider a membrane of surface viscosity μ and Canham-Helfrich's constant $c_{\rm CH}$ that is being pulled from its end by an external axial force F_T. In this particular geometry, the exact problem admits an analytical solution with uniform (independent of $\mathbf{x}$) circumferential and axial stresses. The exact velocity field is given by

$$\mathbf{u} \;=\; U_r\,\check{\mathbf{e}}_r + \chi\, z\,\check{\mathbf{e}}_z \tag{45}$$

with U_r and χ given by

$$U_r \;=\; -\frac{1}{8\pi\mu}\left[F_T \;-\; 2\pi c_{\rm CH}\frac{1}{R}\left(1+\frac{p\,R^3}{c_{\rm CH}}\right)\right], \tag{46}$$

$$\chi \;=\; \frac{1}{8\pi\mu R}\left[F_T \;-\; 2\pi c_{\rm CH}\frac{1}{R}\left(1+\frac{p\,R^3}{c_{\rm CH}}\right)\right]. \tag{47}$$

Neglecting the contribution of the internal pressure p, and noticing that

$$\frac{dR}{dt} = U_r \tag{48}$$

one arrives at the more tractable equation

$$\frac{dR}{dt} \;=\; \frac{c_{\rm CH}}{4\mu}\left(\frac{1}{R_{\rm eq}} - \frac{1}{R(t)}\right). \tag{49}$$

There exists an *equilibrium radius* $R_{\rm eq}$ given by

$$R_{\rm eq} \;=\; \frac{2\pi c_{\rm CH}}{F_T}, \tag{50}$$

to which the cylinder will tend as $t \to \infty$. At equilibrium, the surface pressure $\pi_{\rm s}$ takes the value

$$\pi_{\rm s,eq} = -\frac{F_T}{4\pi R_{\rm eq}} = -\frac{F_T^2}{8\pi^2 c_{\rm CH}}.$$

Further, the final decay when $R \simeq R_{\rm eq}$ must have the asymptotic behavior

$$R(t) = R_{\rm eq} + \; C \; \exp\left(-\frac{c_{\rm CH}}{4\,\mu\,R_{\rm eq}^2}\; t\right). \tag{51}$$

The characteristic relaxation time is

$$\mathcal{T} = \frac{4\,\mu\,R_{\rm eq}^2}{c_{\rm CH}} = \frac{16\,\pi^2\,\mu\,c_{\rm CH}}{F_T^2}$$

For t much greater than τ the tether is expected to be at equilibrium following a rigid-body translation along the line of F_T. The material deforms to take the shape of a cylinder in the region to the left of point "b" in Figure 5, which is approximately fixed in space (the "beginning" of the tether). Once the material enters the tether it simply moves at constant velocity along it. The "end" of the tether (point "e") moves at a constant velocity U_T determined by a balance between the applied force and the viscous stresses at the connection region between the tether and the membrane body.

Going back to non-dimensional quantities, the equilibrium radius and the tether relaxation time are given by

$$R_{\rm eq} = \frac{2\,\pi}{F_T} \qquad \text{and} \qquad \mathcal{T} = \frac{16\,\pi^2}{F_T^2} \tag{52}$$

5.3.2. Numerical tweezers

We have implemented numerical tweezers as a model for the external surface force $\mathbf{f}$. Each numerical tweezer has a radius r_T, which is fixed in time, while the position of its center follows a path described by the vectors $\mathbf{x}_T^0$, $\mathbf{x}_T^1$, etc.

Given a point $\mathbf{x}$ in $\mathbb{R}^3$, the tweezer's penetration at point $\mathbf{x}$ and time t_{n+1}, denoted by $w^{n+1}(\mathbf{x})$, is defined as

$$w^{n+1}(\mathbf{x}) \stackrel{\text{def}}{=} r_T - \|\mathbf{d}_T^{n+1}(\mathbf{x})\|$$

where

$$\mathbf{d}_T^{n+1}(\mathbf{x}) \stackrel{\text{def}}{=} \mathbf{x} - \mathbf{x}_T^{n+1}$$

The repulsive force that the tweezer exerts on $\mathbf{x}$ depends exponentially on $w^{n+1}(\mathbf{x})$, according to

$$\mathbf{f}^{n+1}(\mathbf{x}) = k_T \frac{e^{w^{n+1}(\mathbf{x})/\ell_T}}{\|\mathbf{d}_T^{n+1}(\mathbf{x})\|} \mathbf{d}_T^{n+1}(\mathbf{x})$$

In an exact setting, this force would be integrated over $\mathbf{x} \in \Gamma^{n+1}$. Unfortunately, this force is needed at the time of computing $\mathbf{u}_h^{n+1}$ through (34), and thus the integral is performed over Γ^n. One could replace $\mathbf{f}^{n+1}$ by $\mathbf{f}^n$ in (34), but the following approximation has much more stable behavior:

$$\mathbf{f}^{n+1}(\mathbf{x}) = k_T \frac{e^{w^{n+1}(\mathbf{x})/\ell_T}}{\|\mathbf{d}_T^{n}(\mathbf{x})\|} \mathbf{d}_T^{n}(\mathbf{x}) - k_T \frac{\delta t\, e^{w^{n}(\mathbf{x})/\ell_T}}{\ell_T \|\mathbf{d}_T^{n}(\mathbf{x})\|^2} (\mathbf{d}_T^{n}(\mathbf{x}) \otimes \mathbf{d}_T^{n}(\mathbf{x}))\ \mathbf{u}_h^{n+1}(\mathbf{x}) \qquad (53)$$

Notice that the last term in (53) is an implicit linearization that must be added to the matrix arising from the left-hand side of (34). The two parameters k_T and ℓ_T are given the values 10^5 and $r_T/50$, respectively.

The numerical tweezer can be moved specifying either the velocity or the total force exerted on the membrane. In the former case, the update rule is simply

$$\mathbf{x}_T^{n+1} = \mathbf{x}_T^n + \delta t\, \mathbf{U}_T^{n+1}$$

where $\mathbf{U}_T$ is the specified tweezer velocity. In cases where the force is specified, a simple proportional feedback controler was implemented that adjusts $\mathbf{U}_T^{n+1}$ so as to keep the force at the target value.

Figure 6 illustrates our tweezing strategy, depicting a situation in which six tweezers are simultaneously pushing a membrane outwards, from within.

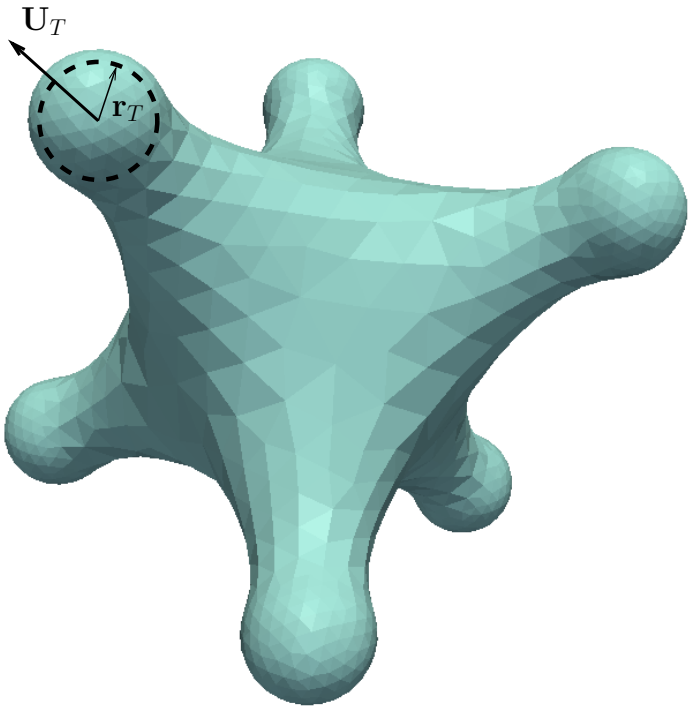

Figure 6: An illustration of the tweezing strategy. In this case six tweezers are simultaneously acting on a membrane.

5.3.3. Dynamical effects in tweezing

The viscous-flow model presented here can deal, unlike gradient-flow models, with dynamical effects in excursions away from equilibrium. An illustrative application is the analysis of velocity effects in tether development carried below.

Let us consider an equilibrium oblate shape corresponding to a reduced volume $v = 0.6666$. A tweezer of constants

$$r_T = 0.04, \qquad k_T = 10^5, \qquad \ell_T = \frac{r_T}{50}$$

is placed at $\mathbf{x}_T(t = 0)$ on the interior of the surface, close to it, and is moved at constant velocity U_T along the outward normal direction. The simulations are run until a time T such that the tweezer displacement $D_T = \|\mathbf{x}_T(T) - \mathbf{x}_T(0)\| = U_T\, T = 1.0$, meaning a non-dimensional displacement of the tweezer of 1.0 for all cases. We have observed that it is necessary to reduce the time step for the tweezing simulations. Specifically, δt is now chosen as

$$\delta t \;=\; \frac{1}{4}\,\delta t^*(h_{\min}) \tag{54}$$

and the results are confirmed by re-running the simulation with one half of this value.

Since the goal is to consider just the interaction of one tweezer, the rigid motions are filtered out by Lagrange multipliers just as in the free relaxation cases.

The resulting membrane shapes at different positions of the tweezer, indicated by its displacement D_T, and for several values of the tweezer velocity U_T are shown in Figure 7.

The leftmost column of the figure corresponds to the smallest velocity, $U_T = 1$. In this case, the membrane deforms almost quasistatically, without showing any localized response at the tweezer's location. As the velocity is increased to $U_T = 10$ one begins to "see" the tweezer pushing outwards from within the membrane. But it is only for $U_T = 100$ and $U_T = 1000$ that the small size of the tweezer ($r_T = 0.04$) becomes apparent and the tweezer produces a tethering-like deformation.

Considering just the bottom row of Figure 7, for which the tweezer position is exactly the same (and the center of mass of the membrane too, thanks to the rigid-motion filtering), the

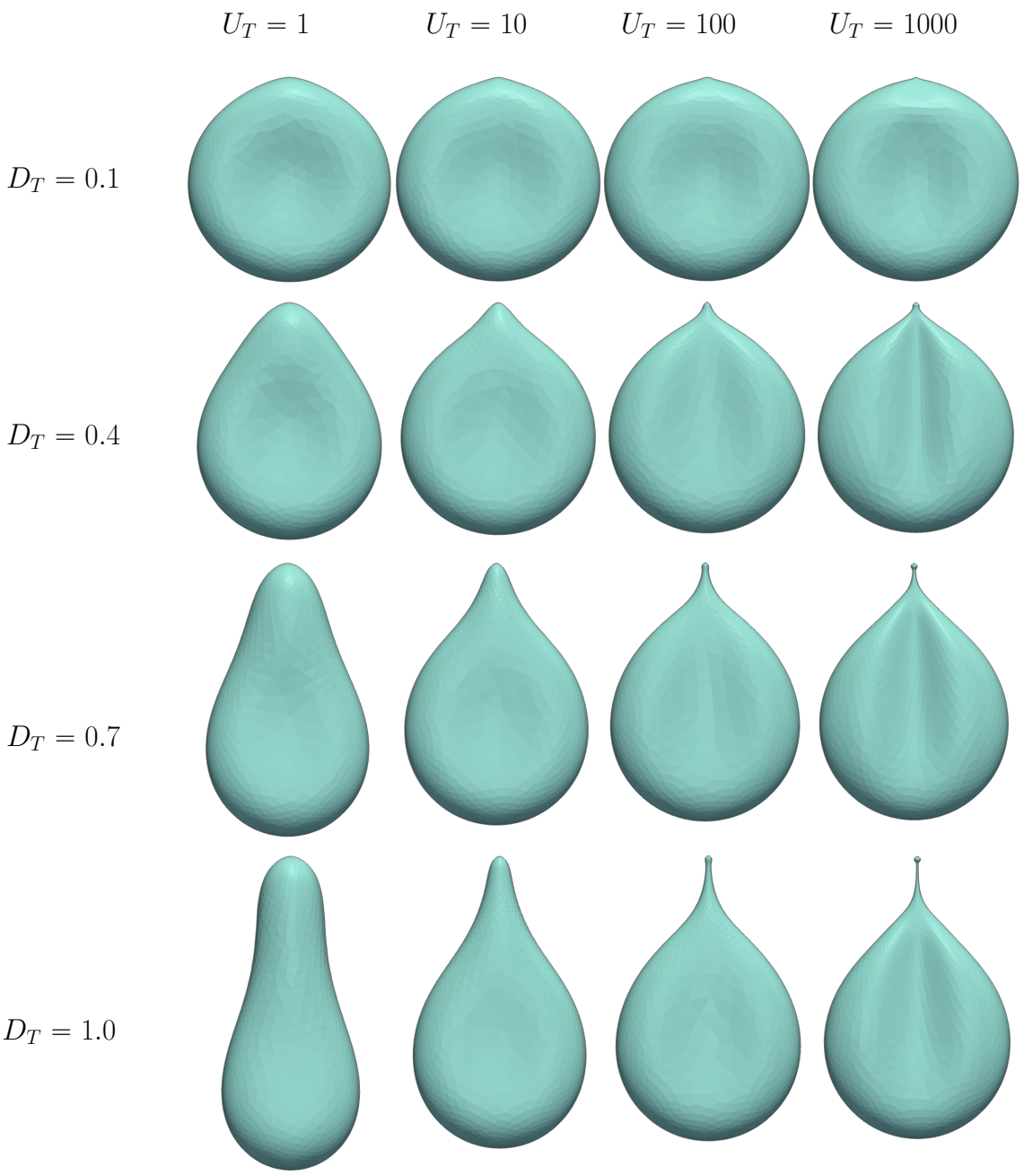

Figure 7: Dynamical effects in tweezing. Deformation of an equilibrium oblate shape with $v = 0.6666$ by a tweezer of radius $r_T = 0.04$ moving outwards at constant velocity U_T (vertically). Shown are the membrane shapes for four values of the tweezer's displacement $D_T = 0.1$, 0.4, 0.7 and 1.0, and for $U_T = 1$, 10, 100 and 1000.

ability of the proposed method to capture velocity-dependent deformations of the membrane is evident.

5.3.4. Tether dynamical equilibrium

We now assess the ability of the method to correctly predict the dynamical equilibrium of the tether. For that purpose, we take a tether formed by applying a tweezer force of $F_T = 400$ and suddenly change the force. Two runs were performed, in one of them F_T is changed to 500 and in the other to 600. The time is redefined to be zero at the time of the force change. The mesh is adapted and remeshed using $c_h = 1/2$, which is rather coarse ($h \simeq R_{\text{eq}}/2$). The time step is adjusted according to (54).

By post-processing the mesh it is possible to compute the radius of the tether as a function of time, as shown in Fig. 8. The initial exact equilibrium radius is $R_{\text{eq}}(F_T = 400) = 0.0157$, which is reasonably approximated by the method despite the mesh being quite coarse.

After changing the force to $F_T = 500$, the tether's radius shrinks to a value of approximately 0.013, which is a good approximation to $R_{\text{eq}}(F_T = 500) = 0.0126$. Further, the evolution towards the new radius is in good agreement with an exponential of the form $a\, e^{-t/\mathcal{T}} + b$, where $\mathcal{T} = 6.32 \times 10^{-4}$ is given by (52), as shown by a continuous line in the figure.

A similar procedure is conducted for the change to $F_T = 600$, for which the exact values are $R_{\text{eq}}(F_T = 600) = 0.0105$ and $\mathcal{T} = 4.39 \times 10^{-4}$.

The relaxation towards the equilibrium radius is seen to agree quite well with the analytical solution (though better for $F_T = 500$ than for $F_T = 600$), and the equilibrium radius itself is predicted with an error of about 5%. This error level is reasonable, considering that there are just about twelve elements in the tether's circumference.

5.3.5. Complex tweezing

This last section reports on a more complex tweezing experiment which aims at testing the robustness of the proposed method. Starting from a spherical membrane of area $4\,\pi$ (i.e., taking as R_0 the radius of the initial sphere), six independent tweezers of radius $r_T = 0.1$

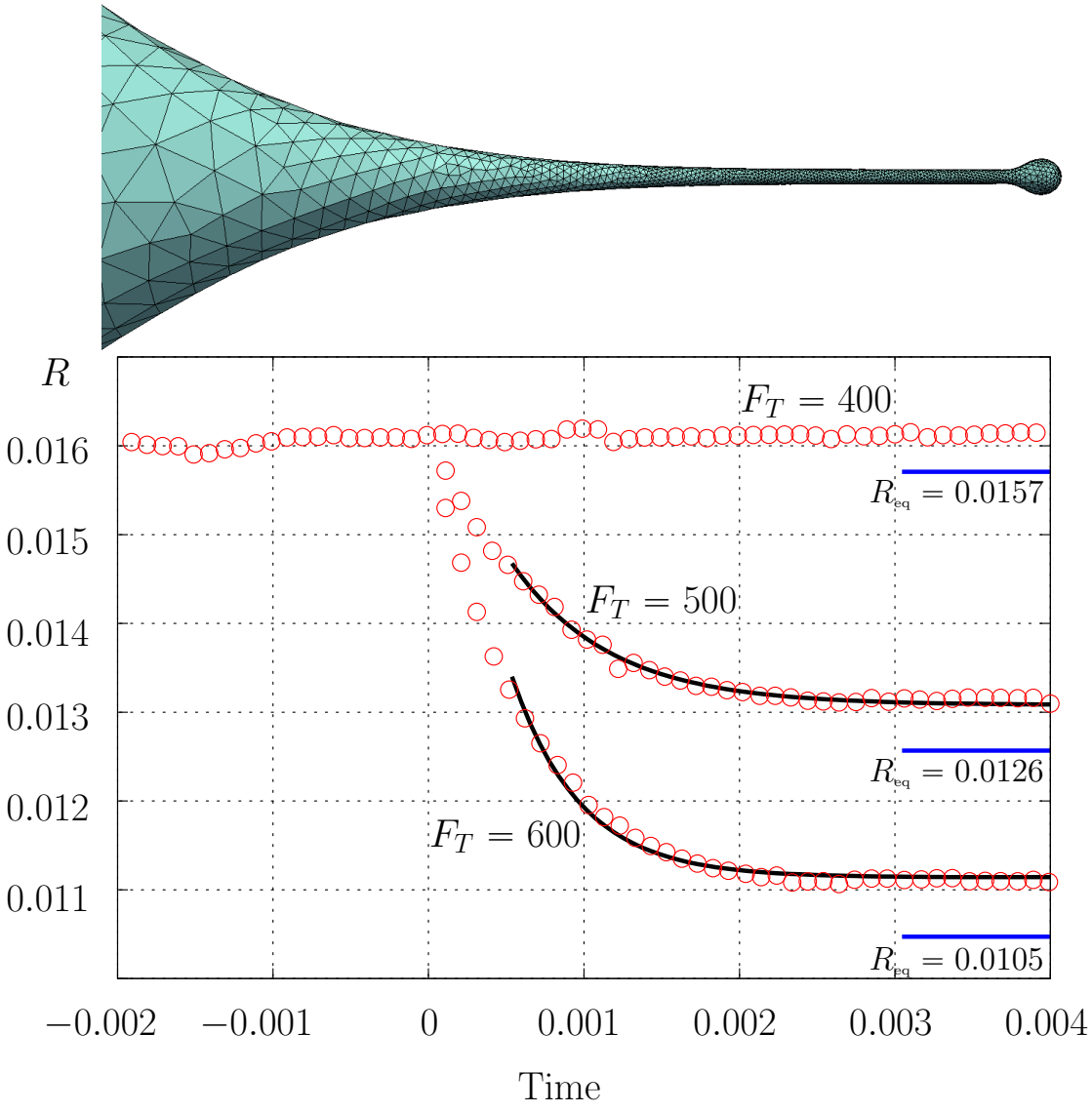

Figure 8: Response of the tether's radius to a sudden change in the tweezer's force. From a tether in dynamical equilibrum at $F_T = 400$, the force is changed to $F_T = 500$ or $F_T = 600$ at $t = 0$. The circles correspond to the numerical results obtained with the proposed method. The black lines correspond to an exponential adjustment with characteristic time given by (52). On the right the exact equilibrium radius (as given by (52) is shown with a short blue segment.

move radially outwards with $U_T = 100$ acting upon it. The tweezers initial positions are the intersection of the membrane with the six cartesian semi-axes.

Though the imposed values of area, $\mathcal{A}^*$, and volume, $\mathcal{V}^*$, were introduced as constants, in this experiments they are set as specified functions of time,

$$\mathcal{A}^*(t) = 4\pi + 400\,t \tag{55}$$

$$\mathcal{V}^*(t) = \frac{4\pi}{3} - 50\,t \tag{56}$$

A time-dependent enclosed volume may result from a variable osmotic pressure in the fluid that surrounds the membrane, while a time-dependent area may result from the incorporation of lipids to the membrane.

Along the simulation, the time step was continually adjusted according to

$$\delta t = 0.105\,h_{\min}^2$$

and the remeshing procedure was applied automatically, with $c_h = 0.5$.

A picture of the membrane's evolution can be seen in Fig. 9. The tweezers are seen to "emerge" from the sphere first deforming the membrane into an approximate octahedron (at time ~ 0.005) and then further stretching the octahedron into a star-like shape. Though there exist mechanisms that may create protrusions such as those in Fig. 9 in actual cells or lipidic vesicles [41, 42], this case does not attempt to model a specific physical phenomenon.

In Fig. 10 plots of several variables of the simulation can be found. The energy is seen to increase monotonically along the deformation, with the area and volume following their target values $\mathcal{A}^*(t)$ and $\mathcal{V}^*(t)$ quite closely. The forces exerted by each of the six tweezers are also plotted in Fig. 10. They differ from one another until at $t \simeq 0.005$ the membrane tightens and all the tweezers start behaving alike.

Notice the strong perturbations introduced by remeshing, which are the result of slight changes in the penetration of each tweezer by the interpolatory construction of the new mesh. The algorithm is able to recover itself from these strong perturbations quite rapidly.

Finally, let us provide some computational data of this simulation. The time step and the minimum element size $h_{\min}$ are plotted as functions of time in Fig. 11. Also shown are

the shape and size qualities of the mesh, Q_{shape} and Q_{size}, as functions of time in Fig. 12. The initial mesh consists of 2160 elements and 1082 nodes, while the final one consists of 5128 elements and 2566 nodes. The complete simulation comprises 1525 time steps, which take 29 minutes on an i7-based laptop at 2.8 GHz. The linear system is solved by LU factorization using the MUMPS package [43, 44], with a memory requirement of 2 GBytes.

6. CONCLUSIONS

In this contribution, we have introduced a fully discrete semi-implicit finite element scheme for the simulation of viscous membranes with bending elasticity of the Canham-Helfrich type. The membrane is discretized by a surface mesh made up of planar triangles, over which a mixed formulation (velocity-curvature) is built with P_1 interpolants for all fields. Two stabilization terms are incorporated in the discrete formulation: The first one stabilizes the inextensibility constraint by a pressure-gradient-projection scheme [30], the second couples curvature and velocity to improve temporal stability[33]. The volume constraint is handled by a Lagrange multiplier (which turns out to be the internal pressure), and an analogous strategy is used to filter out rigid-body motions. Feedback controllers are used to avoid drifting from imposed values of enclosed volume and total area. The nodal positions are updated in a Lagrangian manner and automatic remeshing strategy maintains suitable refinement and mesh quality throughout the simulation.

The method has been numerically assessed through extensive relaxation and tweezing experiments. For the latter, a specific virtual tweezing algorithm was devised. It has been shown that the proposed method is convergent and robust, though with a severe (of order h^2) stability restriction on the time step for which a practical estimate was derived. This stability restriction is the main difficulty in the applications of the algorithm, since it makes thousands of time steps necessary for the simulation of relatively simple membrane motions.

Another difficulty still encountered, though currently avoided by quality-based automatic remeshing, is the existence of small persistent velocities at the numerical equilibrium which slowly but continually deteriorate the mesh quality.

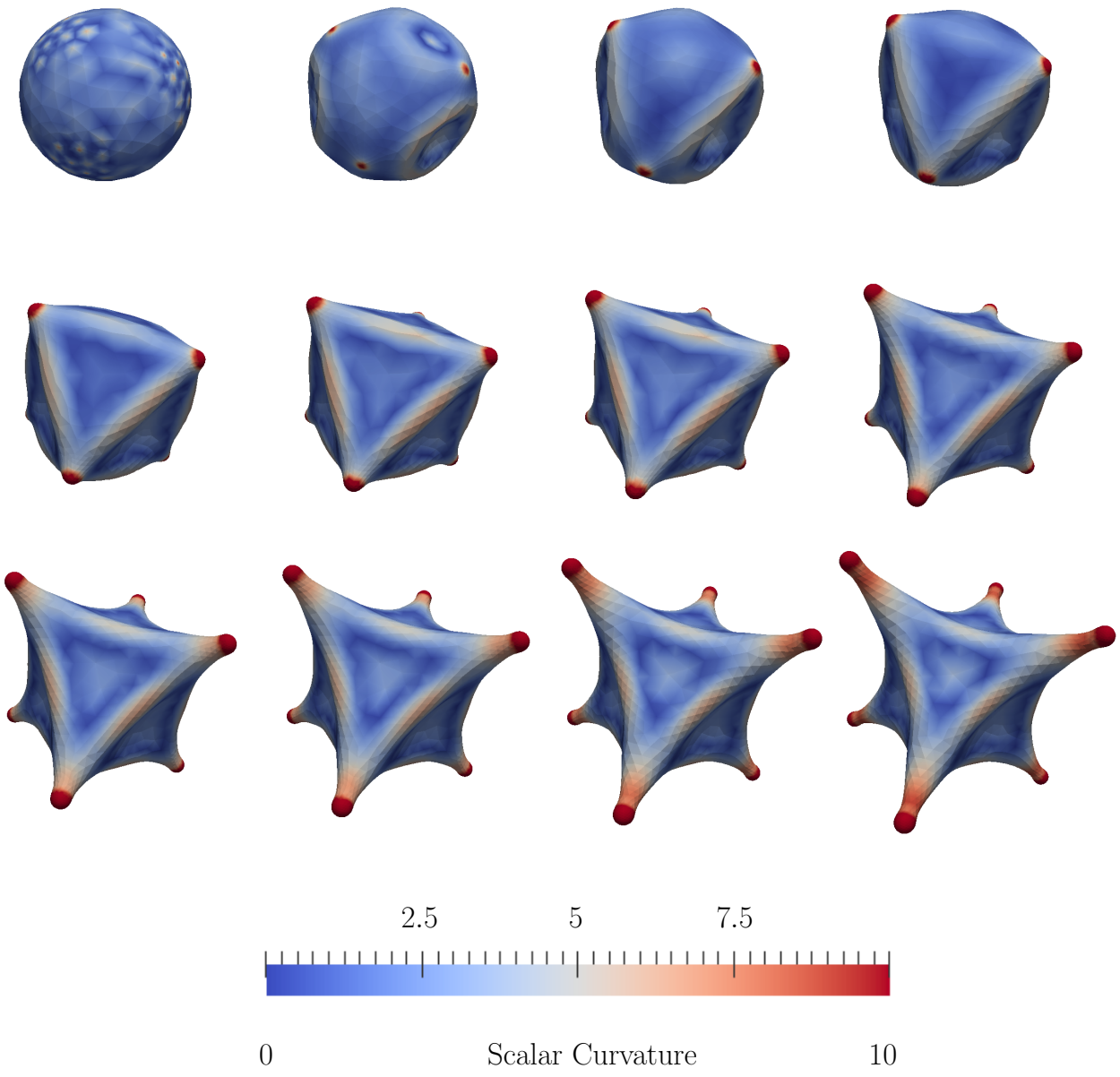

Figure 9: Evolution of the membrane's shape along the "complex tweezing" simulation. Shown are snapshots of the shape at equispaced time intervals of 0.8×10^{-3} time units. The shapes are shaded according to the value of the scalar curvature.

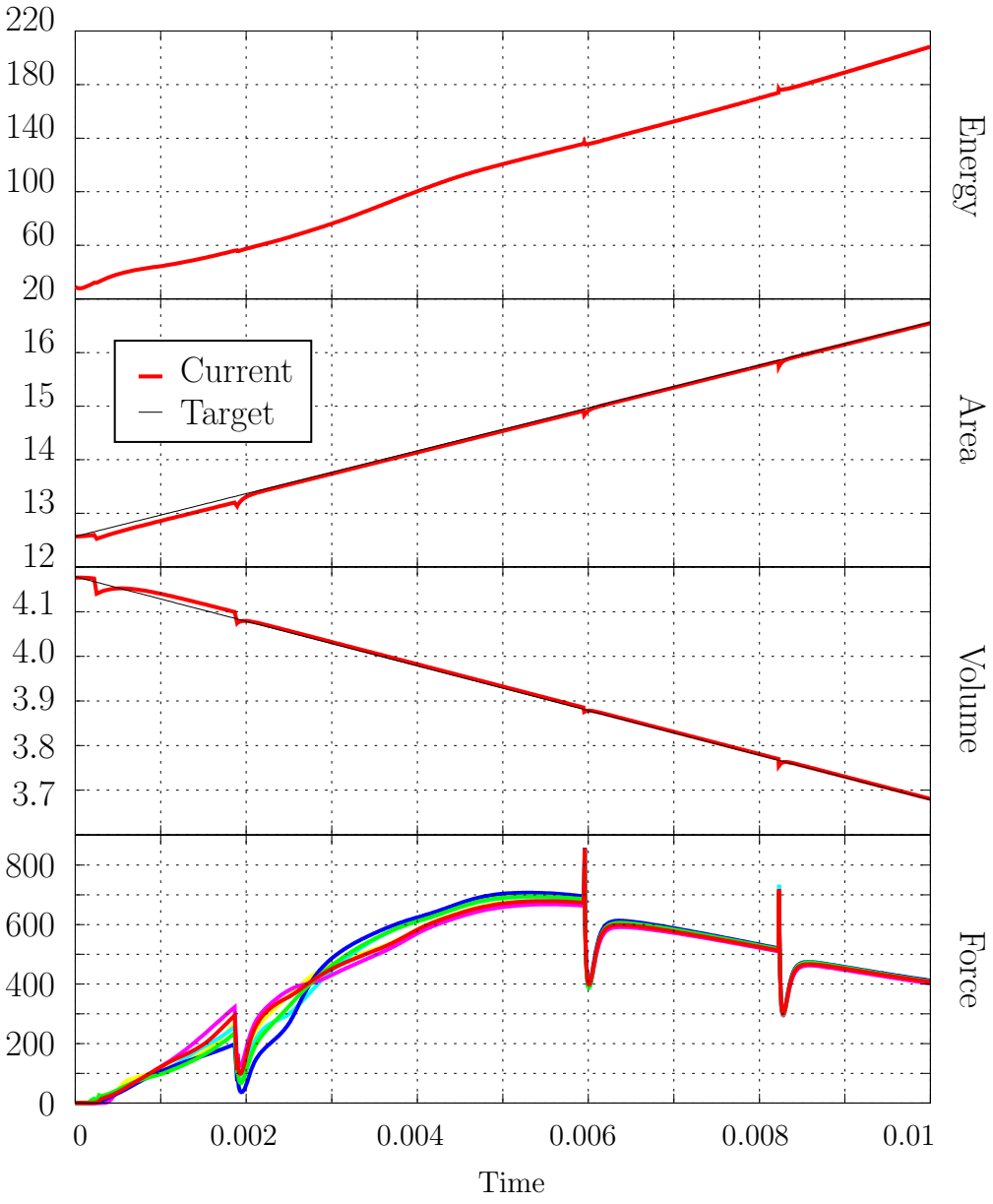

Figure 10: Plots of energy, area, volume and tweezer forces (the six of them) as functions of time as obtained in the "complex tweezing" simulation.

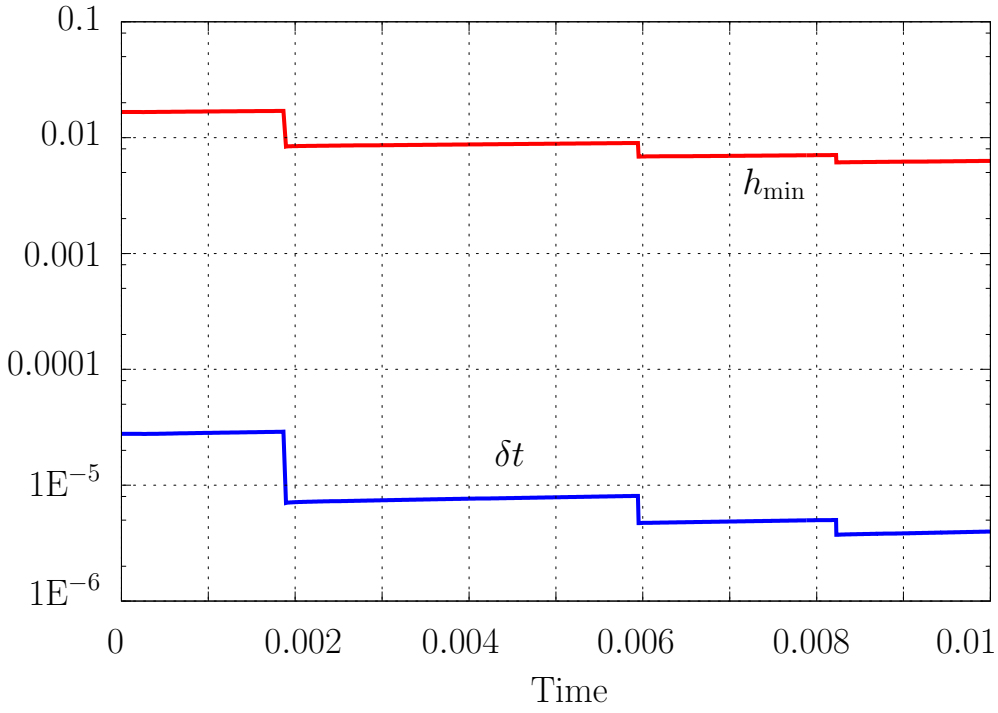

Figure 11: Plots of δt and $h_{\min}$ as functions of time in the "complex tweezing" simulation.

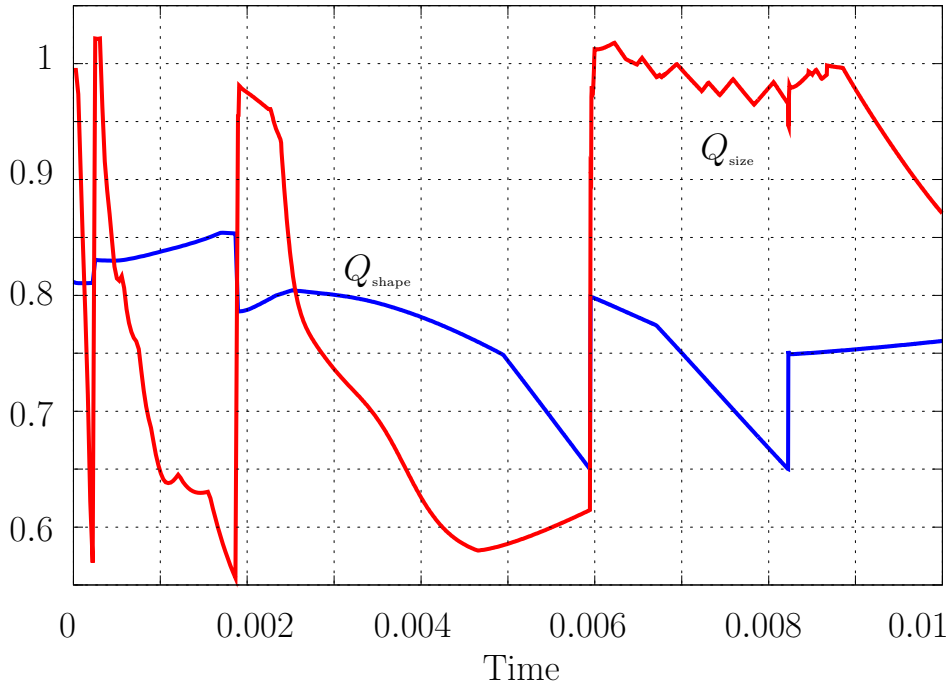

Figure 12: Plots of Q_{shape} and Q_{size} as functions of time in the "complex tweezing" simulation.

ACKNOWLEDGMENTS

The authors gratefully acknowledge the financial support received from São Paulo Research Foundation (FAPESP, grants. no. 2011/01800-5, 2012/14481-8 and 2012/23383-0) and from the Brazilian National Research and Technology Council (CNPq).

References

[1] B. Alberts, D. Bray, K. Hopkin, A. Johnson, J. Lewis, M. Raff, K. Roberts, P. Walter, Essential Cell Biology, NY Garland Science, New York, 2010.

[2] P. Canham, The minimum energy of bending as a possible explanation of the biconcave shape of the human red blood cell, J. Theor. Biol. 26 (1970) 61–81.

[3] U. Seifert, Configurations of fluid membranes and vesicles, Advances in Physics 46 (1997) 13–137.

[4] G. Dziuk, Computational parametric willmore flow, Numer. Math. 111 (2008) 55–80.

[5] R. Rusu, An algorithm for the elastic flow of surfaces, Interfaces Free Boundaries 7 (2005) 229–239.

[6] F. Feng, W. Klug, Finite element modeling of lipid bilayer membranes, J. Comput. Phys. 220 (2006) 394–408.

[7] J. Barrett, H. Garcke, R. Nürnberg, Parametric approximation of willmore flow and related geometric evolution equations, SIAM J. Scientific Computing 31 (2008) 225–253.

[8] A. Bonito, R. Nochetto, M. Pauletti, Parametric FEM for geometric biomembranes, J. Comp. Phys. 229 (2010) 3171–3188.

[9] A. Bonito, R. Nochetto, S. Pauletti, Dynamics of biomembranes: Effect of the bulk fluid, Math. Model. Nat. Phenom. 6 (22) (2011) 25–43.

[10] C. Elliott, B. Stinner, Modeling and computation of two phase geometric biomembranes using surface finite elements, J. Comp. Phys. 229 (2010) 6585–6612.

[11] C. Harland, M. Bradley, R. Parthasarathy, Phospholipid bilayers are viscoelastic, Proc. Nat. Acad. Sci. USA 107 (2010) 19146–19150.

[12] C. Harland, M. Bradley, R. Parthasarathy, Retraction, Proc. Nat. Acad. Sci. USA www.pnas.org/cgi/doi/10.1073/pnas.1111381108.

[13] M. Arroyo, A. DeSimone, Relaxation dynamics of fluid membranes, Physical Review E 79 (2009) 031915 (17 pages).

[14] L. Scriven, Dynamics of a fluid interface. equations of motion for newtonian surface fluids, Chem. Eng. Sci. 12 (1960) 98–108.

[15] M. Arroyo, A. DeSimone, L. Heltai, The role of membrane viscosity in the dynamics of fluid membranes, Tech. rep., arXiv:1007.4934v1 (2010).

[16] M. Rahimi, M. Arroyo, Shape dynamics, lipid hydrodynamics, and the complex viscoelasticity of bilayer membranes, Physical Review E 86 (2012) 011932 (15 pages).

[17] I. Tasso, G. Buscaglia, A finite element method for viscous membranes, Computer Methods in Applied Mechanics and Engineering 255 (1) (2013) 226 – 237.

[18] H. J. Lee, E. L. Peterson, R. Phillips, W. S. Klug, P. A. Wiggins, Membrane shape as a reporter for applied forces, Proceedings of the National Academy of Sciences 105 (49) (2008) 19253–19257. arXiv: http://www.pnas.org/content/105/49/19253.full.pdf+html, doi:10.1073/pnas.0806814105.
URL http://www.pnas.org/content/105/49/19253.abstract

[19] A.-S. c. v. Smith, E. Sackmann, U. Seifert, Pulling tethers from adhered vesicles, Phys. Rev. Lett. 92 (2004) 208101. doi:10.1103/PhysRevLett.92.208101.
URL http://link.aps.org/doi/10.1103/PhysRevLett.92.208101

[20] R. Waugh, Surface viscosity measurements from large bilayer vesicle tether formation I: analysis, Biophys. J. 38 (1982) 19–27.

[21] B. Bozic, S. Svetina, B. Zeks, Theoretical analysis of the formation of membrane microtubes on axially strained vesicles, Phys. Rev. E 55 (1997) 5834–5842.

[22] R. Waugh, Surface viscosity measurements from large bilayer vesicle tether formation II: experiments, Biophys. J. 38 (1982) 29–37.

[23] G. C. Buscaglia, R. F. Ausas, Variational formulation for surface tension, capillarity and wetting, Comput. Methods Appl. Mech. Engrg. 200 (2011) 3011–3025.

[24] A. Biria, M. Maleki, E. Fried, Continuum theory for the edge of an open lipid bilayer, Adv. Applied Mech. 46 (2013) 1–68.

[25] S. Gross, A. Reusken, Numerical Methods for Two-phase Incompressible Flows,, Springer Series in Computational Mathematics, Vol. 40, 2011.

[26] P. Rangamani, A. Agrawal, K. Mandadapu, G. Oster, D. Steigmann, Interaction between surface shape and intra-surface viscous flow on lipid membranes, Biomech. Model. Mechanobiol. 12 (2013) 833–845.

[27] W. Helfrich, Elastic properties of lipid bilayers – theory and possible experiments, Zeitschrift für Naturforschung C 28 (1973) 693–703.

[28] T. J. Willmore, Riemannian Geometry, Claredon Press, Oxford, 1993.

[29] E. Evans, A. Yeung, Hidden dynamics in rapid changes of bilayer shape, Chemistry and Physics of Lipids 73 (1994) 39–56.

[30] R. Codina, J. Blasco, A finite element formulation for the Stokes problem allowing equal velocity-pressure interpolation, Computer Methods in Applied Mechanics and Engineering 143 (1997) 373–391.

[31] G. Buscaglia, F. Basombrío, R. Codina, Fourier analysis of an equal-order incompressible flow solver stabilized by pressure-gradient projection, Int. J. Numer. Meth. in Fluids 34 (2000) 65–92.

[32] R. Codina, J. Blasco, G. Buscaglia, A. Huerta, Implementation of a stabilized finite element formulation for the incompressible navier-stokes equations based on a pressure gradient projection, Int. J. Numer. Meth. in Fluids 37 (2001) 410–444.

[33] E. Bänsch, Finite element discretization of the Navier–Stokes equations with a free capillary surface, Numer. Math. 88 (2001) 203–235.

[34] R. Lohner, Regridding surface triangulations, Journal of Computational Physics 126 (1) (1996) 1 – 10.

[35] S. K. Veerapaneni, R. Raj, G. Biros, P. Purohit, Analytical and numerical solutions for shapes of quiescent two-dimensional vesicles, Inter. Jour. Non-Linear Mech. 44 (3) (2009) 257–262.

[36] S. Ganesan, G. Matthies, L. Tobiska, On spurious velocities in incompressible flow problems with interfaces, Comput. Methods Appl. Mech. Engrg. 196 (2007) 1193–1202.

[37] S. Gross, A. Reusken, An extended pressure finite element space for two-phase incompressible flows with surface tension, J. Comput. Phys. 224 (2007) 40–58.

[38] A. Reusken, Analysis of an extended pressure finite element space for two–phase incompressible flows, Comput. Visual. Sci. 11 (2008) 293–305.

[39] S. Popinet, An accurate adaptive solver for surface–tension–driven interfacial flows, J. Comput. Phys. 228 (2009) 5838–5866.

[40] R. Ausas, F. Sousa, G. Buscaglia, An improved finite element space for discontinuous pressures, Computer Meth. Appl. Mech. Engng. 199 (2010) 1019–1031.

[41] D. Fygenson, J. Marko, A. Libchaber, Mechanics of microtubule-based membrane extension, Physical Review Letters 79 (1997) 4497–4500.

[42] M. Staykova, M. Arroyo, M. Rahimi, H. Stone, Confined bilayers passively regulate shape and stress, Physical Review Letters 110 (2013) 028101.

[43] P. R. Amestoy, I. S. Duff, J. Koster, J.-Y. L'Excellent, A fully asynchronous multifrontal solver using distributed dynamic scheduling, SIAM Journal on Matrix Analysis and Applications 23 (1) (2001) 15–41.

[44] P. R. Amestoy, A. Guermouche, J.-Y. L'Excellent, S. Pralet, Hybrid scheduling for the parallel solution of linear systems, Parallel Computing 32 (2) (2006) 136–156.